

RESEARCH ARTICLE OPEN ACCESS

Structural Health Monitoring of Thin Shell Structures

Ihtisham Khalid¹ | Zahid Ahmed Qureshi¹ | Faisal Siddiqui¹ | Selda Oterkus² | Erkan Oterkus² ¹Department of Aerospace Engineering, College of Aeronautical Engineering, National University of Sciences & Technology, Islamabad, Pakistan | ²Department of Naval Architecture, Ocean & Marine Engineering, University of Strathclyde, Glasgow, Scotland, UK**Correspondence:** Erkan Oterkus (erkan.oterkus@strath.ac.uk)**Received:** 28 October 2024 | **Revised:** 17 November 2024 | **Accepted:** 21 November 2024**Keywords:** defect | iFEM | inverse shell element | shape sensing | structural health monitoring | thin plate and shell

ABSTRACT

Thin plate and shell structures are extensively used in aerospace, naval, and energy sectors due to their lightweight and efficient load-bearing properties. Structural Health Monitoring (SHM) implementations are becoming increasingly important in these industries to reduce maintenance costs, improve reliability, and ensure safe operations. This study presents an efficient triangular inverse shell element for thin shell structures, developed using discrete Kirchhoff assumptions within the inverse finite element method (iFEM) framework. The proposed inverse formulation is efficient and requires fewer strain sensors to achieve accurate and reliable displacement field reconstruction than existing inverse elements based on the First Order Shear Deformation Theory (FSDT). These features are critical to iFEM-based SHM strategies for improving real-time efficiency while reducing project costs. The inverse element is rigorously validated using benchmark problems under in-plane, out-of-plane, and general loading conditions. Also, its performance is compared to an existing competitive inverse shell element based on FSDT. The inverse formulation is further evaluated for robust shape-sensing capability, considering a real-world structural configuration under a practicable sparse sensor arrangement. Additional investigation includes defect characterization and structural health assessment using damage index criteria. This research contributes toward developing more reliable and cost-effective monitoring solutions by highlighting the potential application of the proposed inverse element for SHM frameworks designed for thin shell structures.

1 | Introduction

Structural health monitoring (SHM) has become an essential tool across various industrial sectors, offering modern solutions to enhance maintenance efficiency, improve safety, and reduce costs. By collecting and analyzing real-time sensory data, SHM systems enable accurate predictions of structural behavior and facilitate early detection of damage, such as cracks, delamination, or corrosion. Traditional inspection methods, like visual or ultrasonic testing, while effective, can be labor-intensive, time-consuming, and may not always detect obscured damage. A key challenge in SHM is its ability to continuously monitor structural integrity in real time. Rather than relying solely on point-wise measurements, full-field reconstruction of displacement and stress profiles is critical for comprehensive

health assessments. This approach allows for identifying and quantifying defects that might otherwise go undetected.

Rapid sensor technology advancements have significantly transformed SHM applications in recent years. Traditional techniques have evolved into sophisticated, real-time intelligent sensing systems for structural health prognosis. Based on their core methodologies, SHM methods are broadly classified into two categories: data-driven and model-based approaches [1]. Data-driven approaches, particularly those utilizing deep neural networks (DNNs), offer considerable advantages in reconstructing complex structural behavior [2, 3]. These robust frameworks can effectively address both forward and inverse analyses, making them highly suitable for SHM applications. However, they are data-intensive, requiring substantial computational resources and a machine learning (ML)

This is an open access article under the terms of the [Creative Commons Attribution](https://creativecommons.org/licenses/by/4.0/) License, which permits use, distribution and reproduction in any medium, provided the original work is properly cited.

© 2025 The Author(s). *International Journal of Mechanical System Dynamics* published by John Wiley & Sons Australia, Ltd on behalf of Nanjing University of Science and Technology.

framework [4, 5]. Despite these challenges, DNN-based methods present promising alternatives for SHM, especially when traditional mechanical approaches struggle to capture intricate structural responses [1]. In contrast, model-based methods are typically more robust and efficient, using physics-based structural models to detect and assess damage while predicting structural responses to potential future loading conditions. However, the full-field reconstruction of structural behavior poses an inverse problem that has intrigued researchers for their significant contributions to the evolution of accurate shape-sensing technologies.

Early research in full-field displacement reconstruction began with Ko's Displacement Theory [6], which enabled the reconstruction of wing-bending profiles using limited onboard sensors. Ko et al. [7] used the Euler–Bernoulli beam theory to reconstruct wing deflections by strategically placing strain sensors along the wing span. However, the simplified assumptions of the beam theory limit its effectiveness in capturing complex behaviors, such as shear and torsional effects, reducing its applicability for structures with intricate geometries and loading conditions. Consequently, while effective for beam-like structures, extending this approach to built-up structures requires accounting for more complex deformation modes, such as membrane stresses or buckling. Furthermore, Ko's approach struggles to detect localized effects, such as damages, in real-world SHM applications.

Other researchers, such as Foss and Haugse [8], have explored global and piecewise continuous basis functions for displacement reconstruction. The Modal Transformation Theory [9, 10] also attracted attention for reconstructing displacement profiles from normal mode shapes. However, these methods depend heavily on accurate mode shape data, which can be compromised by material degradation or structural damage. Additionally, limited modes in these methods can overlook localized deformations, a critical factor in SHM applications. Shkarayev [11] introduced a two-step least-squares method for displacement reconstruction. This approach estimates the applied load on the structure and then determines the displacement field. Consequently, the reliability of the reconstructed displacements depends considerably on the accuracy of these load predictions. Even minor errors in load estimations can lead to significant inaccuracies in the reconstructed displacement profiles.

More recently, variational and model-based approaches have become increasingly popular for full-field displacement reconstruction. Tessler [12] introduced the inverse finite element method (iFEM), which uses a variational error functional using discrete onboard strain data to reconstruct displacement profiles without relying on material properties or loading conditions. This framework is advantageous in real-world scenarios, offering a more reliable method for reconstructing displacements than traditional techniques, which require precise material and loading information. Also, the iFEM framework can handle diverse structural configurations and is reliable against sparse strain data, making it an essential tool for shape-sensing and SHM applications [13].

Various inverse elements developed for specific structural needs have since expanded the versatility of iFEM. Tessler and Spangler [14] introduced the iMIN3 element for full-field shape-sensing applications. Similarly, Kefal et al. [15] developed the

iQS4 element for SHM in the naval sector, later developing a curved inverse element (iCS8) for marine structures [16]. Khalid et al. [17] proposed the iKP4 element using non-conforming Hermite basis functions for thin plates. Higher-order isogeometric inverse elements [18, 19] have also been developed to address complex geometries, improving interelement compatibility. De Mooij et al. [20] extended iFEM to thick structures with a 3D solid inverse element, and the i3-RZT element [21] advanced the iFEM capabilities for composite laminates and sandwich structures. Khalid et al. recently introduced an inverse crack tip element (iTP6) to perform iFEM analysis on structures with pre-existing cracks and reconstruct crack mechanics [22].

Numerous inverse elements in the literature are based on the first order shear deformation theory (FSDT), used for iFEM analysis of thin and thick shell structures. For thicker structures, shear correction factors are applied, and transverse shear strains are calculated using FSDT equilibrium equations. In dealing with thin shell structures, the transverse shear strain computations are neglected; however, this assumption does not improve computational efficiency since the shear deformation terms are integral to the inverse formulation. Another challenge of FSDT-based elements is shear locking in analyzing thin structures due to the dominance of transverse shear deformation terms. Additionally, these elements tend to converge slowly for thin plates and shells, requiring a large number of strain sensors. As a result, FSDT-based inverse elements face difficulties in accurately analyzing thin structures, leading to high computational costs and impractically large sensor requirements. The literature emphasizes that the effectiveness of the iFEM shape-sensing capability is closely linked to the kinematic assumptions in the inverse formulation. Therefore, an efficient inverse shell element explicitly designed for thin shell structures is needed for efficient SHM applications, reducing overall project costs.

This study proposes a new triangular inverse shell element (iKS3) for SHM applications, designed to overcome the limitations of existing FSDT-based formulations for thin shell structures. The iKS3 formulation is straightforward, neglecting transverse shear effects based on discrete Kirchhoff assumptions. It also integrates hierarchical drilling rotation to improve compatibility and extend its use to complex built-up structures. In contrast to FSDT-based elements, the iKS3 formulation is computationally efficient, simple to implement, and free from locking issues when applied to thin plates and shells. A rigorous numerical validation, using well-known benchmark problems, assesses the performance of the iKS3 element. Comparative analysis with the iMIN3 inverse shell element evaluates its accuracy and efficiency in reconstructing displacement fields. For SHM applications, the robustness of the iKS3 element is tested on the curved stiffened panel commonly found in airframes and barges. Additionally, the damage detection capabilities of the iKS3 inverse shell element are assessed for material degradation defects.

The rest of this article is organized as follows: Section 2 presents the inverse shell formulation and theoretical background. Detailed mathematical aspects, including shape functions for triangular elements, drilling rotation degree of freedom (DOF), and discrete Kirchhoff bending fields, are outlined in Appendices A–C. Appendix D describes the coordinate

transformation system essential for shell formulations. Section 3 provides benchmark results and compares iFEM results for the iKS3 and iMIN3 elements. Section 4 discusses SHM applications considering real-world cases, including displacement reconstruction, defect detection, and damage assessment. Finally, the conclusion summarizes the key findings and the importance of the study for efficient and cost-effective SHM applications involving thin plate and shell structures.

2 | Formulation of the Inverse Shell Element

According to the kinematics of the classical plate theory (CPT), Kirchhoff-based elements require C^1 continuity in the deflection field due to the presence of second derivatives of deflection in the virtual work expression. Achieving this level of continuity requires special techniques, such as using Hermite basis functions, which increases computational complexity, particularly when analyzing built-up structures [23].

To address the strict continuity requirements, Batoz et al. [24] proposed the Discrete Kirchhoff Theory. This method simplifies the problem by applying the Kirchhoff hypothesis only along the element edges, relating the rotations to transverse displacements. This approach enables using more straightforward C^0 continuity elements while ensuring convergence to the Kirchhoff plate theory solution. The formulation neglects transverse shear energy, consistent with the thin plate theory, and relies on the deflection w and rotations (θ_x, θ_y) as the independent variables, which only require C^0 continuity. The Kirchhoff hypothesis discretely relates the rotations to transverse displacements along the element edges, such that $\theta_x = -w_{,y}$ and $\theta_y = w_{,x}$.

A general expression for the strain field, consisting of membrane and bending components, can be written as

$$\boldsymbol{\varepsilon}(\mathbf{u}) = \mathbf{e}(\mathbf{u}) + \boldsymbol{\kappa}(\mathbf{u}), \quad (1)$$

where $\boldsymbol{\varepsilon}(\mathbf{u})$ represents the strain field, $\mathbf{e}(\mathbf{u})$ denotes the membrane strains, and $\boldsymbol{\kappa}(\mathbf{u})$ represents the bending strains associated with bending curvatures. The strain field can further be expressed in terms of its strain components as

$$\boldsymbol{\varepsilon}(\mathbf{u}) = \begin{Bmatrix} \varepsilon_{xx} \\ \varepsilon_{yy} \\ \gamma_{xy} \end{Bmatrix} = \begin{Bmatrix} \varepsilon_{xx}^o \\ \varepsilon_{yy}^o \\ \gamma_{xy}^o \end{Bmatrix} - z \begin{Bmatrix} \kappa_{xx} \\ \kappa_{yy} \\ \kappa_{xy} \end{Bmatrix}. \quad (2)$$

The strain field for membrane and bending curvatures can be written more conveniently as

$$\mathbf{e}(\mathbf{u}) = \begin{Bmatrix} \varepsilon_{xx}^o \\ \varepsilon_{yy}^o \\ \gamma_{xy}^o \end{Bmatrix} = \begin{Bmatrix} \frac{\partial}{\partial x} & 0 \\ 0 & \frac{\partial}{\partial y} \\ \frac{\partial}{\partial y} & \frac{\partial}{\partial x} \end{Bmatrix} \begin{Bmatrix} u_o \\ v_o \end{Bmatrix}, \quad (3)$$

$$\boldsymbol{\kappa}(\mathbf{u}) = \begin{Bmatrix} \kappa_{xx} \\ \kappa_{yy} \\ \kappa_{xy} \end{Bmatrix} = \begin{Bmatrix} \frac{\partial}{\partial x} & 0 \\ 0 & \frac{\partial}{\partial y} \\ \frac{\partial}{\partial y} & \frac{\partial}{\partial x} \end{Bmatrix} \begin{Bmatrix} \theta_x \\ \theta_y \end{Bmatrix}. \quad (4)$$

In this formulation, $\mathbf{e}(\mathbf{u})$ represents the membrane strains, while $\boldsymbol{\kappa}(\mathbf{u})$ corresponds to the bending curvatures. The independent rotations θ_x and θ_y directly relate to the nodal displacements, maintaining the Kirchhoff element characteristics. These strain–displacement relationships form the basis for the inverse shell formulation using the iFEM weighted least-squares functional.

The constitutive relationship between the non-zero stress and strain states for a homogeneous material under isothermal conditions can be expressed as

$$\boldsymbol{\sigma}(\mathbf{u}) = [\mathbf{C}]\boldsymbol{\varepsilon}(\mathbf{u}) \quad (5)$$

where \mathbf{C} is the constitutive matrix containing the material properties. Following the thin plate theory, the transverse normal and transverse shear stresses σ_{zz} , γ_{yz} , and γ_{zx} are assumed to be zero, simplifying the stress state to the in-plane components. The constitutive matrix for an isotropic material, considering these assumptions, is given by

$$\mathbf{C} = \frac{E}{1-\nu^2} \begin{Bmatrix} 1 & -\nu & 0 \\ -\nu & 1 & 0 \\ 0 & 0 & \frac{1-\nu}{2} \end{Bmatrix} \quad (6)$$

where E is the Young's modulus and ν is the Poisson's ratio. These material properties fully characterize the in-plane response of isotropic materials under the assumptions of the thin plate theory.

To start with finite element approximation, consider a three-node triangular inverse shell element defined in the physical coordinate system (x, y, z) , where the nodes are located at the mid-plane of the shell. The thickness of the shell is represented by $z \in [-t/2, t/2]$, as illustrated in Figure 1. The master element, shown in Figure 2, is defined in the natural barycentric coordinate system (ξ, η) .

The transformation between the physical and natural coordinate systems for the triangular element is achieved using linear shape functions $N_i(\xi, \eta)$, which are functions of the natural barycentric coordinates ξ and η corresponding to the i th node of the triangular element. These shape functions are defined as follows:

$$N_1(\xi, \eta) = 1 - \xi - \eta, \quad (7a)$$

$$N_2(\xi, \eta) = \xi, \quad (7b)$$

$$N_3(\xi, \eta) = \eta. \quad (7c)$$

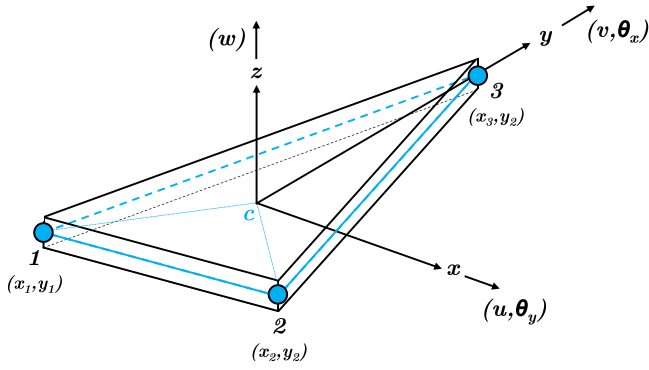


FIGURE 1 | iKS3 defined in the physical coordinate system.

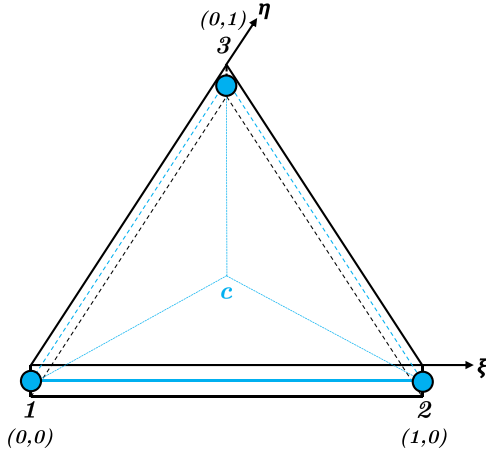


FIGURE 2 | Master element defined in the natural coordinate system.

In this shell formulation, six degrees of freedom (DOF) are associated with each node, encompassing three translational displacements and three rotational components. The nodal displacement vector for the iKS3 inverse shell element is defined as

$$\mathbf{u}_i^e = \begin{bmatrix} (u_o)_i \\ (v_o)_i \\ (w)_i \\ (\theta_x)_i \\ (\theta_y)_i \\ (\theta_z)_i \end{bmatrix} \quad (i = 1, 2, 3). \quad (8)$$

For the i th node of the inverse element, u_o , v_o , w represent the nodal displacements, while θ_x and θ_y denote the bending rotations along the y - and x -axis, respectively. The variable θ_z corresponds to the drilling rotation, a hierarchical DOF introduced to enhance element compatibility. Originally proposed by Allman [25], drilling DOF are particularly beneficial in preventing coplanar singularities in complex built-up structures. During iFEM-based shape-sensing analysis, these unknown nodal displacements are reconstructed using discrete strain measurements obtained from onboard sensors.

The in-plane translational displacement components u and v for the triangular inverse shell element are defined using the linear

shape functions from Equation (7) along with contributions from the drilling DOF θ_z :

$$u = \sum_{i=1}^3 N_i(\xi, \eta) u_{o_i} + \sum_{i=1}^3 L_i(\xi, \eta) \theta_{z_i}, \quad (9)$$

$$v = \sum_{i=1}^3 N_i(\xi, \eta) v_{o_i} + \sum_{i=1}^3 M_i(\xi, \eta) \theta_{z_i}, \quad (10)$$

where $L(\xi, \eta)$ and $M(\xi, \eta)$ are anisoparametric shape functions that incorporate the effect of the drilling DOF θ_z , and their explicit forms are provided in Appendix B.

The membrane nodal variable vector \mathbf{U}_i^m , consisting of both displacements and drilling rotation at each node, is expressed as

$$\mathbf{u}_i^m = \begin{bmatrix} (u_o)_i \\ (v_o)_i \\ (\theta_z)_i \end{bmatrix} \quad (i = 1, 2, 3), \quad \mathbf{u}^m = \begin{bmatrix} \mathbf{u}_1^m \\ \mathbf{u}_2^m \\ \mathbf{u}_3^m \end{bmatrix}, \quad (11)$$

where \mathbf{u}^m represents the complete membrane displacement field for the element. The elemental strain $\mathbf{e}(\mathbf{u}^e)$ for the membrane formulation can be calculated by substituting Equations (9) and (10) into the strain–displacement relationship, as shown in Equation (12):

$$\mathbf{e}(\mathbf{u}^e) = \mathbf{B}^m \mathbf{u}^e, \quad (12)$$

where \mathbf{B}^m is the membrane strain–displacement gradient matrix and \mathbf{u}^e is the displacement vector for the element. The nodal membrane gradient matrix \mathbf{B}_i^m for node i is given as

$$\mathbf{B}_i^m = \begin{bmatrix} \frac{\partial N_i}{\partial x} & 0 & 0 & 0 & 0 & \frac{\partial L_i}{\partial x} \\ 0 & \frac{\partial N_i}{\partial y} & 0 & 0 & 0 & \frac{\partial M_i}{\partial y} \\ \frac{\partial N_i}{\partial y} & \frac{\partial N_i}{\partial x} & 0 & 0 & 0 & \frac{\partial M_i}{\partial x} + \frac{\partial L_i}{\partial y} \end{bmatrix}. \quad (13)$$

By assembling the nodal gradient matrices \mathbf{B}_i^m for each node ($i = 1, 2, 3$), the overall membrane gradient matrix \mathbf{B}^m for the element is obtained as

$$\mathbf{B}^m = [\mathbf{B}_1^m \quad \mathbf{B}_2^m \quad \mathbf{B}_3^m]. \quad (14)$$

The bending gradient matrix formulation for the proposed inverse shell element is derived from the discrete Kirchhoff triangular (DQT) bending element, as initially presented by Batoz et al. [24]. The derivation of the DQT bending element is well documented in the literature; this discussion focuses on utilizing its displacement field to formulate the bending gradient matrix for the current inverse shell element.

In a linear triangular domain, the independent bending rotations θ_x and θ_y can be approximated using anisoparametric shape functions, consistent with the discrete Kirchhoff hypothesis:

$$\theta_x = \mathbf{H}^x(\xi, \eta)^T \mathbf{u}^b, \quad (15)$$

$$\theta_y = \mathbf{H}^y(\xi, \eta)^T \mathbf{u}^b, \quad (16)$$

where $\mathbf{H}^x(\xi, \eta)$ and $\mathbf{H}^y(\xi, \eta)$ are shape function vectors that map the element displacement field \mathbf{u}^b to the bending rotations θ_x and θ_y , respectively. Both $\mathbf{H}^x(\xi, \eta)$ and $\mathbf{H}^y(\xi, \eta)$ comprise nine anisoparametric shape functions, as introduced by Batoz et al. [24], and their explicit definitions, derived from the standard quadratic basis functions of the six-node triangular element, can be found in Appendix A. The expressions for the shape function vectors \mathbf{H}^x and \mathbf{H}^y are provided in Appendix C.

The bending nodal variables \mathbf{u}_i^b can be organized to represent the bending displacement field for the element as follows:

$$\mathbf{u}_i^b = \begin{bmatrix} (w)_i \\ (\theta_x)_i \\ (\theta_y)_i \end{bmatrix} (i = 1, 2, 3), \mathbf{u}^b = \begin{bmatrix} \mathbf{u}_1^b \\ \mathbf{u}_2^b \\ \mathbf{u}_3^b \end{bmatrix}, \quad (17)$$

where \mathbf{u}^b represents the complete bending displacement field of the element. The numerical elemental strains $\boldsymbol{\kappa}(\mathbf{u}^e)$ for the bending part can be computed using Equations (15) and (16) in the strain-displacement relationship:

$$\boldsymbol{\kappa}(\mathbf{u}^e) = \mathbf{B}^b \mathbf{u}^e, \quad (18)$$

where \mathbf{B}^b denotes the element bending gradient matrix. The nodal bending gradient matrix \mathbf{B}_i^b is expressed in terms of the shape functions \mathbf{H}^x and \mathbf{H}^y as follows:

$$\mathbf{B}_i^b = \begin{bmatrix} 0 & 0 & \mathbf{H}_{j+1,x}^x & \mathbf{H}_{j+2,x}^x & \mathbf{H}_{j+3,x}^x & 0 \\ 0 & 0 & \mathbf{H}_{j+1,y}^y & \mathbf{H}_{j+2,y}^y & \mathbf{H}_{j+3,y}^y & 0 \\ & & \mathbf{H}_{j+1,x}^y & \mathbf{H}_{j+2,x}^y & \mathbf{H}_{j+3,x}^y & \\ 0 & 0 & + & + & + & 0 \\ & & \mathbf{H}_{j+1,y}^x & \mathbf{H}_{j+2,y}^x & \mathbf{H}_{j+3,y}^x & \end{bmatrix}, \quad (19)$$

where $j = 3(i - 1)$, for $i = 1, 2, 3$

where bending gradient matrix \mathbf{B}^b for the entire element is obtained by assembling \mathbf{B}_i^b for each node ($i = 1, 2, 3$) of the iKS3 inverse shell element:

$$\mathbf{B}^b = [\mathbf{B}_1^b \quad \mathbf{B}_2^b \quad \mathbf{B}_3^b]. \quad (20)$$

The iFEM framework is based on the principle of the variational method, where the displacement field is reconstructed by minimizing a weighted least-squares error functional. This functional is formulated using discrete strain measures and their corresponding numerical counterparts in a discretized geometric space. One significant advantage of the iFEM approach is its independence from material properties, such as elasticity or inertia, and loading conditions for full-field shape reconstruction.

The weighted least-squares functional for the proposed iKS3 element is defined as the sum of the error terms between the

numerical and discrete strain measures for membrane and bending strains as

$$\phi^e(\mathbf{u}^e) = w_e \|\mathbf{e}(\mathbf{u}^e) - \mathbf{e}^*\|^2 + w_k \|\boldsymbol{\kappa}(\mathbf{u}^e) - \boldsymbol{\kappa}^*\|^2. \quad (21)$$

where $\mathbf{e}(\mathbf{u}^e)$ and $\boldsymbol{\kappa}(\mathbf{u}^e)$ represent the numerically computed membrane and bending strains, while \mathbf{e}^* and $\boldsymbol{\kappa}^*$ are the in situ discrete strain measures obtained from strain sensors located within the geometric domain of the inverse element. w_e and w_k are the weighting coefficients associated with the squared norms corresponding to membrane and bending strain errors, respectively. The squared norms from Equation (21) can be expressed over the inverse element domain Ω^{iel} as

$$\|\mathbf{e}(\mathbf{u}^e) - \mathbf{e}^*\|^2 = \iint_{A_e} (\mathbf{e}(\mathbf{u}^e) - \mathbf{e}^*)^2 dx dy, \quad (22)$$

$$\|\boldsymbol{\kappa}(\mathbf{u}^e) - \boldsymbol{\kappa}^*\|^2 = t^2 \iint_{A_e} (\boldsymbol{\kappa}(\mathbf{u}^e) - \boldsymbol{\kappa}^*)^2 dx dy, \quad (23)$$

where A_e is the area of an inverse element.

Discrete strain sensor measurements obtained from onboard strain sensors are critical to the iFEM formulation. These experimental strains are evaluated at discrete locations (x_j, y_j) within an inverse element at its mid-plane, as shown in Figure 3. For general loading conditions and complex structures, strain sensors on both surfaces (top and bottom) are needed to compute accurate section strains. However, in special cases, such as plane stress or pure bending, strain data from one surface can suffice for iFEM analysis. The in situ strain data typically collected from onboard sensors can be expressed as

$$\mathbf{e}^* = \frac{1}{2} \begin{Bmatrix} \epsilon_{xx}^+ + \epsilon_{xx}^- \\ \epsilon_{yy}^+ + \epsilon_{yy}^- \\ \gamma_{xy}^+ + \gamma_{xy}^- \end{Bmatrix}, \quad (24)$$

$$\boldsymbol{\kappa}^* = \frac{1}{t} \begin{Bmatrix} \epsilon_{xx}^+ - \epsilon_{xx}^- \\ \epsilon_{yy}^+ - \epsilon_{yy}^- \\ \gamma_{xy}^+ - \gamma_{xy}^- \end{Bmatrix}, \quad (25)$$

where \mathbf{e}^* and $\boldsymbol{\kappa}^*$ are the discrete strain measures at location (x_j, y_j) within the spatial domain of an inverse element. Superscripts (+) and (-) indicate top and bottom surface strain data, respectively.

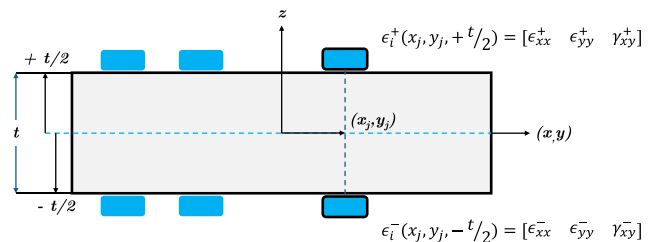


FIGURE 3 | Strain rosettes at discrete locations $(x_j, y_j, \pm t/2)$.

The weighting coefficients w_e and w_k , defined in Equation (21), are selected based on the availability of strain data for the inverse element. If strain measures (\mathbf{e}^* , $\boldsymbol{\kappa}^*$) are available within an inverse element, the coefficients are set to unity, $w_e = w_k = 1$. If not, minimal values $w_e, w_k \ll 1$ are used. This approach ensures that missing data points do not disproportionately affect the error minimization. During the least-squares error minimization process, these weighting coefficients help to balance the influence of available discrete strain measures in the closed-form solution. Setting the coefficients to unity ($w_e = w_k = 1$) gives equal importance to all data points, which are known with certainty when the strain measures are available. On the other hand, setting the coefficients to a minimal value ($w_e = w_k = 10^{-3}$ to 10^{-6}) when the strain data are missing reduces the impact of these missing data points during the error minimization process, preventing them from unduly affecting the overall result. This approach helps to ensure that the iFEM algorithm shows its intended robustness for real-world SHM applications.

Minimizing the least-squares error functional in Equation (21) with respect to unknown nodal displacements \mathbf{u}^e of an inverse element yields the conventional system of the linear equations:

$$\frac{\partial \phi^e(\mathbf{u}^e)}{\partial \mathbf{u}^e} = \mathbf{k}^e \mathbf{u}^e - \mathbf{f}^e = 0, \quad (26)$$

$$\mathbf{k}^e \mathbf{u}^e = \mathbf{f}^e, \quad (27)$$

where \mathbf{k}^e is the shape matrix for the numerical strains, \mathbf{f}^e is the force vector derived from discrete strain measures, and \mathbf{u}^e is the unknown element displacements. The detailed expressions for \mathbf{k}^e and \mathbf{f}^e are as follows:

$$\mathbf{k}^e = \iint_{A_e} \left(w_e (\mathbf{B}^m)^T \mathbf{B}^m + (t^2) w_k (\mathbf{B}^b)^T \mathbf{B}^b \right) dx dy, \quad (28)$$

$$\mathbf{f}^e = \iint_{A_e} \left(w_e (\mathbf{B}^m)^T \mathbf{e}^* + (t^2) w_k (\mathbf{B}^b)^T \boldsymbol{\kappa}^* \right) dx dy. \quad (29)$$

The global system of equations is assembled from the element contributions:

$$\mathbf{K} \mathbf{U} = \mathbf{F}, \quad (30)$$

where \mathbf{K} is the global stiffness matrix, \mathbf{U} is the global displacement vector, and \mathbf{F} is the global force vector. These matrices are assembled as

$$\mathbf{K} = \sum_{e=1}^{N_{iel}} \mathbf{T}^e \mathbf{T}^e (\mathbf{k}^e) \mathbf{T}^e, \quad (31)$$

$$\mathbf{U} = \sum_{e=1}^{N_{iel}} \mathbf{T}^e \mathbf{T}^e (\mathbf{u}^e), \quad (32)$$

$$\mathbf{F} = \sum_{e=1}^{N_{iel}} \mathbf{T}^e \mathbf{T}^e (\mathbf{f}^e). \quad (33)$$

Here, N_{iel} denotes the number of inverse elements, and \mathbf{T}^e is the transformation matrix for each element. Further details on the

element transformation matrix are provided in Appendix D. After applying boundary conditions, the partitioned global system becomes

$$\mathbf{K}_p \mathbf{U}_p = \mathbf{F}_p. \quad (34)$$

Consequently, \mathbf{K}_p , \mathbf{U}_p , and \mathbf{F}_p are the prescribed global inverse stiffness matrix, unknown displacement vector, and global inverse force vector, respectively, in the iFEM formulation. The unknown nodal displacements can then be computed using standard FEM techniques, yielding the full-field displacement reconstruction.

3 | Numerical Validation

The validation of the inverse formulation requires discrete strain data, which can be obtained through two primary methods. First, experimental strain data are obtained using onboard strain sensors. Alternatively, synthetic strain data can be generated via high-fidelity FEM analysis. Under identical loading and boundary conditions, FEM analysis reliably reproduces experimental strain data. As FEM is a well-established analysis tool, the use of synthetic strain data for the numerical validation of inverse formulations is widely accepted within the engineering community. The literature supports this methodology, which has been commonly applied in developing inverse elements [15, 19, 26].

The iFEM formulation for the iKS3 inverse shell element is numerically validated by evaluating key benchmark problems from the literature. A comprehensive validation plan involves assessing the iKS3 element under in-plane (membrane), out-of-plane (bending), and combined loading scenarios for curved shell structures. Numerical modeling is extensively used in research and development to replicate real-world behavior. However, since numerical models like iFEM rely on various assumptions and simplifications, validating them against analytical solutions is critical to ensure their accuracy and reliability. For complex cases where analytical solutions are unavailable, high-fidelity FEM reference solutions provide a dependable comparison for iFEM results.

The numerical cases presented here serve two essential purposes: validating the iKS3 inverse shell element and comparing its performance with the iMIN3 inverse shell element [14]. In both cases, shear deformation effects are neglected when analyzing thin plate and shell structures, which is consistent with the mechanics of such problems [27]. This exclusion is intrinsic in the iKS3 inverse formulation, based on the CPT. The absence of shear deformation terms simplifies the weighted least-squares error functional in iFEM analysis. On the other hand, the iMIN3 formulation includes shear deformation terms and requires the computation of numerical transverse shear strains. Therefore, even if shear deformation effects are disregarded in the iMIN3 element, it does not provide the computational simplicity of the iKS3 formulation, which inherently omits these terms and necessitates fewer strain sensors.

In iFEM applications, numerical validation is typically performed using two sensor configurations: dense and sparse.

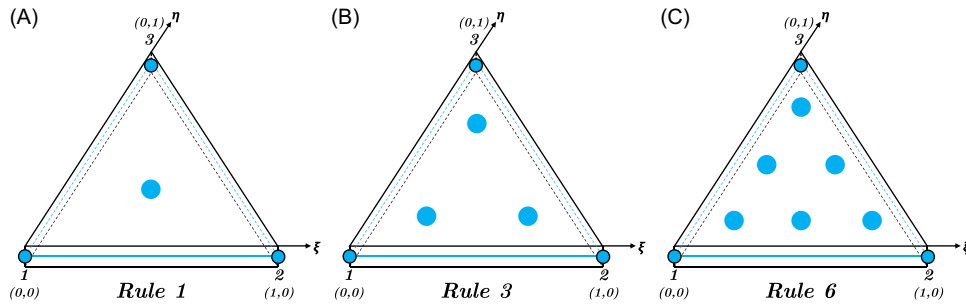


FIGURE 4 | Gauss Locations as per the Gauss Quadrature for triangles in Master Element (A) Rule-1, (B) Rule-2, and (C) Rule-3.

Dense configurations provide strain data for all inverse elements to validate the accuracy of iFEM formulations, while sparse configurations, where strain data are available only for selected inverse elements, assess the robustness of the iFEM algorithm by simulating realistic onboard sensor placements. For straightforward comparison, the numerical validation of iKS3 and iMIN3 elements is conducted using a standardized dense sensor configuration. Another critical factor influencing iFEM accuracy is the location of the strain rosette within the inverse element domain.

In iFEM analysis, the strain rosette can be placed at various positions within the inverse element domain, such as Gauss points, as shown in Figure 4. Structural geometry, loading conditions, and critical stress areas often govern the optimal placement of discrete locations. For this study, the strain rosettes are consistently placed at the center of the inverse element domain (single-point Gauss location) across all validation cases.

3.1 | In-Plane Loading (Case - I)

The plane stress condition represents one of the simplest scenarios in two-dimensional structural analysis. Analytical solutions exist for various problems involving point loads and edge tractions. Several studies [28, 29] have used shear-loaded cantilever beams to assess the membrane behavior of newly developed elements. In this case, this problem is revisited to evaluate the membrane response capabilities of the newly formulated iKS3 inverse shell element.

A rectangular beam with dimensions $b = 1.2192$ m (length), $a = 0.3048$ m (width), and a constant cross-sectional thickness of $t = 25.4$ mm is considered. The left edge is fixed, while the right edge is subjected to a resultant shear load of $P = 177.929$ kN, as illustrated in Figure 5. The beam material is homogeneous and isotropic, with an elastic modulus $E = 206.84$ GPa and Poisson's ratio $\nu = 0.25$. According to the elasticity solution of Timoshenko and Goodier [30], the maximum vertical displacement at the tip of the free edge is given by

$$V = \frac{4Pa^3}{Et b^3} + \frac{2(4 + 5\nu)Pa}{4Et b} = 9.025 \text{ mm.} \quad (35)$$

A high-fidelity FEM analysis is conducted to solve the cantilevered beam benchmark problem. The maximum vertical displacement obtained from the forward FEM analysis is

CASE I : Cantilevered Beam Benchmark

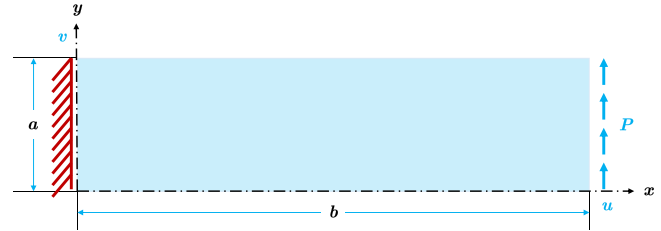


FIGURE 5 | Cantilevered beam - Free edge under shear load.

9.034 mm (as shown in Figure 6A), which aligns well with the analytical solution. The displacement field from the high-fidelity FEM solution is used to generate synthetic discrete strain measures at the centroids of the inverse elements. These discrete strain measures are utilized in the iFEM analysis using the proposed inverse formulation and the iMIN3 inverse element. For membrane problems, strain sensors on either side of the beam generate the required strain data, as the displacement field remains constant through the thickness under in-plane loading conditions.

The iFEM analysis uses two configurations of the iKS3 inverse shell element: one configuration neglects the drilling rotation (θ_z) DOF, given that drilling rotations are hierarchical and can be omitted during analysis. In contrast, the other configuration includes the drilling rotation (θ_z). This approach offers detailed insight into the impact and significance of drilling rotations on the performance of the iKS3 inverse shell element.

The reconstructed vertical displacement profiles for the 24×6 inverse discretization are shown in Figure 6B,C for the iKS3 inverse element, omitting drilling rotations in the former and including them in the latter. Since the membrane formulation is identical for the iKS3 and iMIN3 inverse shell elements, their reconstructed displacement profiles are similar. The absolute error in the reconstruction of the maximum vertical displacement, compared to the analytical solution Equation (35), is 12.17% when drilling rotations are omitted and reduces to 2.86% when drilling rotations are included. However, the reconstructed displacement contours for both configurations are virtually indistinguishable compared to the high-fidelity FEM reference solution shown in Figures 6A.

Figure 7 illustrates the influence of inverse discretization on the reconstruction of the vertical displacement profile. The convergence plot demonstrates the monotonic convergence of the reconstructed displacements for both configurations of the iKS3 inverse element (with and without drilling rotation DOF) and

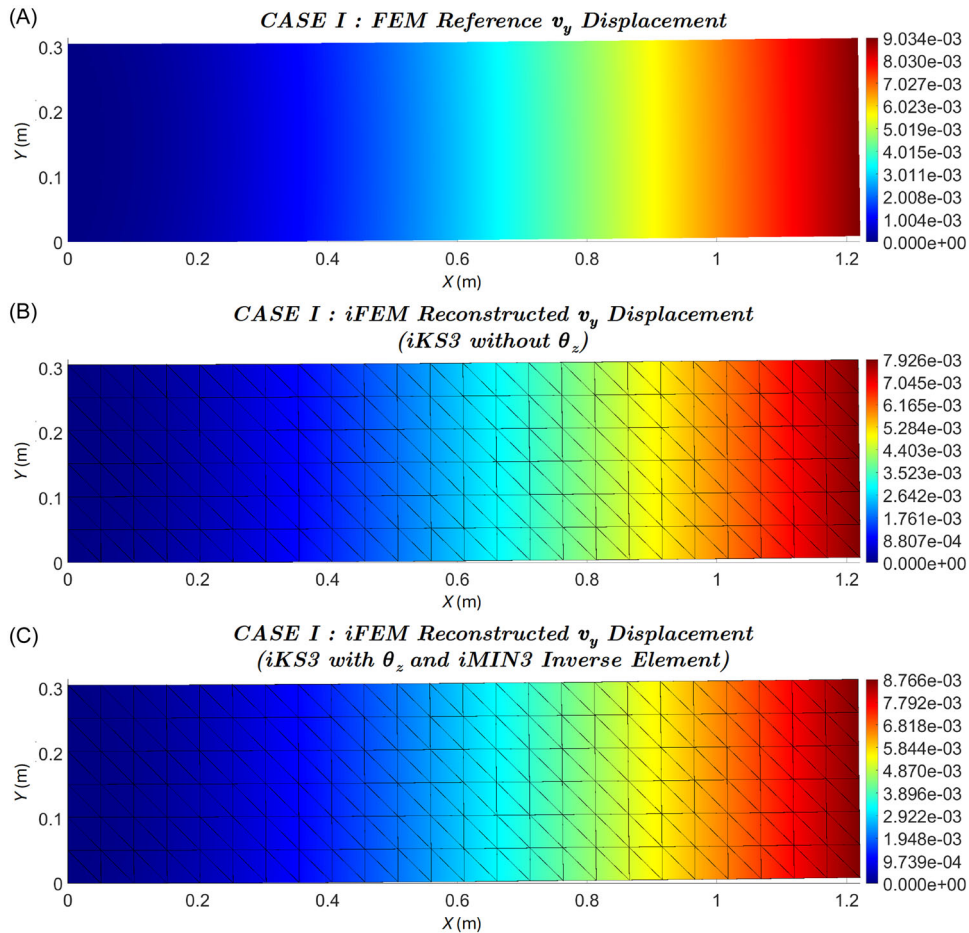


FIGURE 6 | Case I - Vertical displacement profiles: (A) FEM^{Ref}, (B) iFEM iKS3, and (C) iFEM iMIN3.

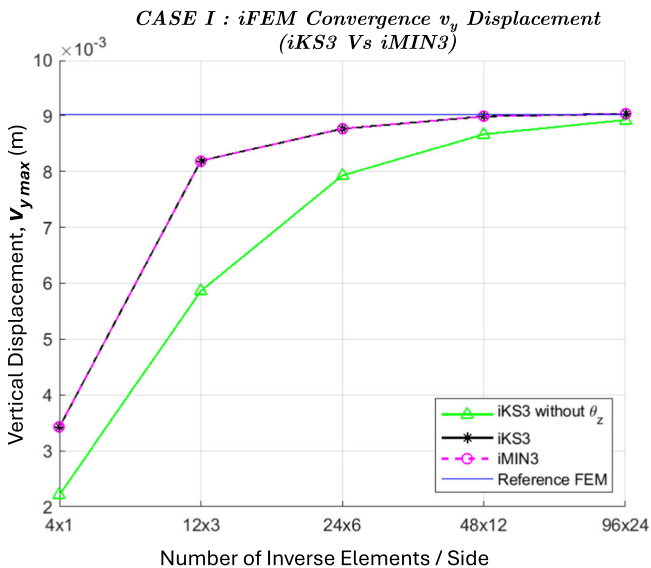


FIGURE 7 | Case I - Influence of inverse discretization on reconstructed vertical displacement.

the iMIN3 inverse element as the number of inverse elements increases. The enhanced membrane response capability of iKS3 and iMIN3 inverse shell elements is due to hierarchical drilling rotation, which improves their ability to capture in-plane rotational effects, resulting in more accurate membrane behavior

and faster convergence. Without drilling rotation DOF, the iFEM results slowly converge to the elasticity solution using more inverse elements, consequently necessitating more on-board strain sensors.

The high-fidelity FEM reference solution in Figure 8A shows the maximum horizontal displacement of 1.636 mm. Reconstructed horizontal displacement contours of iKS3 (with and without drilling rotation DOF) and iMIN3 inverse elements are in close agreement with the high-fidelity FEM reference solution, as shown in Figure 8B,C. The contours accurately reveal the symmetric squeezing and stretching phenomena along the upper and lower edges of the cantilevered beam. When drilling rotations were not included, the iKS3 inverse element reconstructed a maximum horizontal displacement of 1.421 mm (absolute error of 13.14%). Upon including the drilling DOF, both the iKS3 and iMIN3 inverse elements reconstructed a maximum horizontal displacement of 1.583 mm (absolute error of 3.23%).

The iFEM convergence chart presented in Figure 9 illustrates the monotonic convergence of the reconstructed displacements for both configurations of the iKS3 inverse element (with and without drilling rotation DOF) and the iMIN3 inverse element as the number of inverse elements increases. As anticipated, the iKS3 inverse shell element with drilling rotations demonstrates rapid convergence to the reference FEM solution, showing behavior that is identical to that of

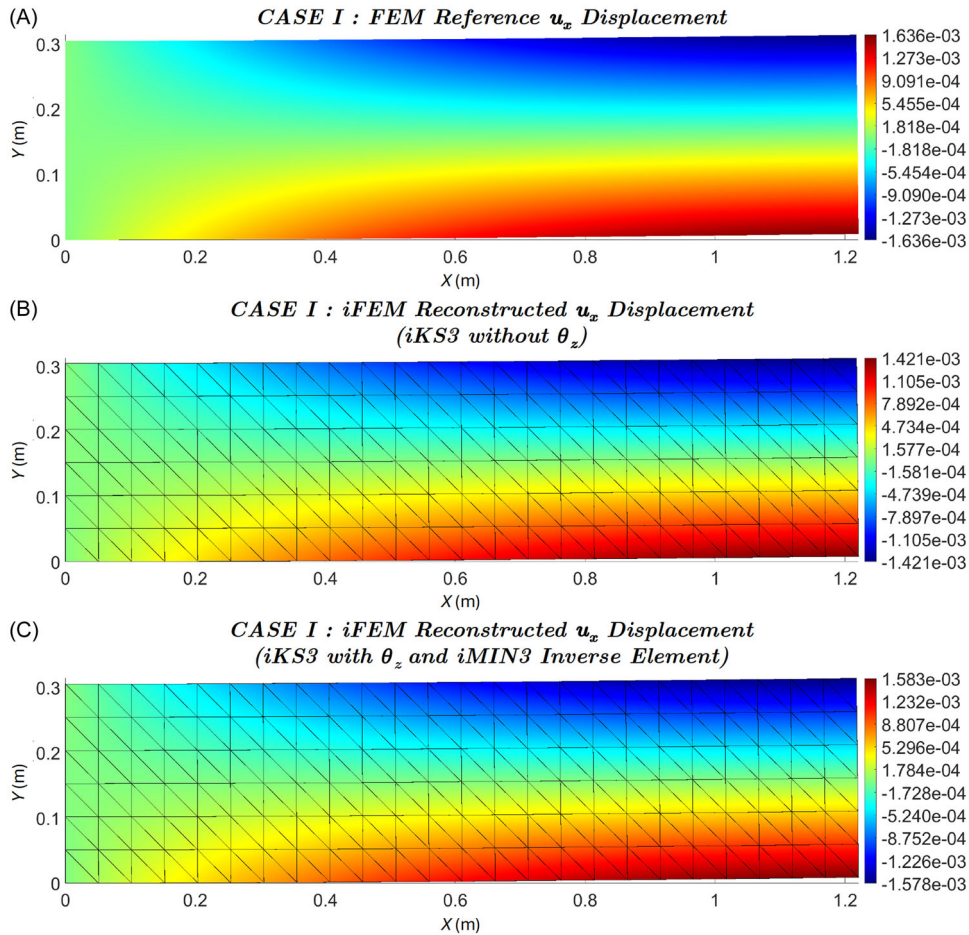


FIGURE 8 | Case I - Horizontal displacement profiles: (A) FEM^{Ref}, (B) iFEM iKS3, and (C) iFEM iMIN3.

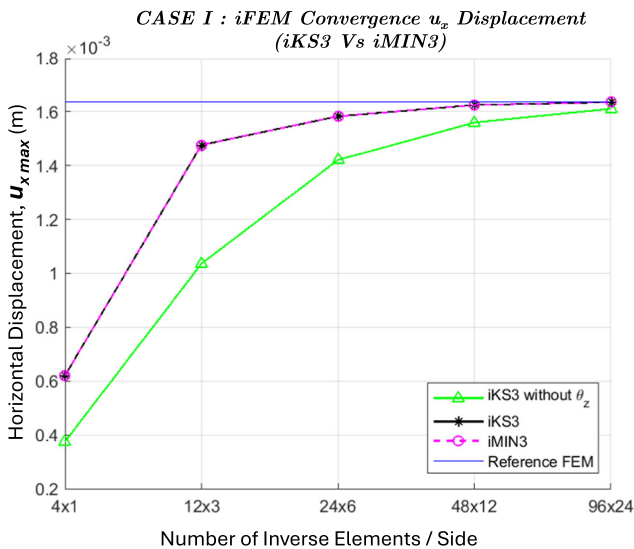


FIGURE 9 | Case I - Influence of inverse discretization on reconstructed horizontal displacement.

the iMIN3 inverse shell element. However, the straightforward inverse formulation of the iKS3 element is computationally more efficient, as its error functional does not require the computation of numerical shear strains. This simplification reduces numerical complexity and incurs less

computational overhead than more complex formulations that account for shear effects. The analysis details for Case-I are summarized in Table 1.

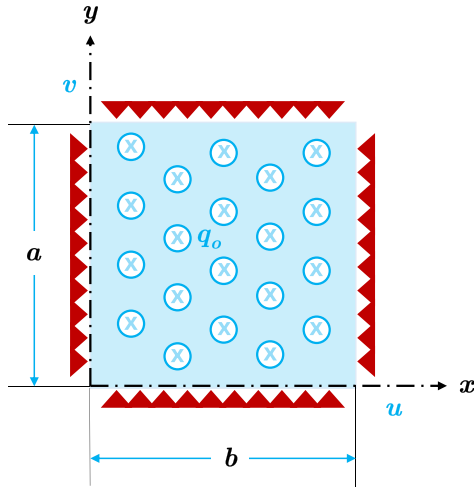
The analysis of the in-plane loading case highlights that the iKS3 element effectively reconstructs horizontal and vertical displacement profiles, achieving accuracy identical to that of the iMIN3 inverse element. Both inverse shell elements incorporate drilling rotation DOF to improve element membrane behavior. However, distinctions in the reconstructed displacements between the iKS3 and iMIN3 elements will emerge in subsequent cases involving bending behavior, as these elements are based on different plate theory assumptions.

3.2 | Out-of-Plane Loading (Case - II)

This benchmark case validates the proposed inverse formulation within the iFEM framework by revisiting a classical pure bending problem from ref [30]. The problem involves an isotropic square plate with supported boundaries, subjected to a uniform transverse pressure q_0 , as shown in Figure 10. The dimensions of the plate (length a , width b , and thickness t) can be chosen arbitrarily since the validation uses dimensionless parameters, where $a = b = c$ and $t \ll c$, where c represents the characteristic length of the plate.

TABLE 1 | Analysis details of Case - I.

Analysis	Sensors	Max v_y	Max u_x	Error [v_y]
Reference FEM	-----	9.034 mm	1.636 mm	0.09% (abs)
iFEM-iKS3	24×8	8.766 mm	1.583 mm	2.86% (abs)
iFEM-iMIN3	24×8	8.766 mm	1.583 mm	2.86% (abs)
Analytical solution [30]		9.025 mm		

CASE II : Plate Bending Benchmark**FIGURE 10** | Simply supported square plate under an arbitrary uniform transverse load.

For this case, a square plate with $a = b = 1$ m is subjected to a uniform transverse pressure of $q_o = 10$ kN. The plate's thickness is set to $t = 0.01$ m, with material properties $E = 200$ GPa and $\nu = 0.3$. The maximum dimensionless transverse deflection at the center of the plate is given by ref [30] as

$$\bar{w}_{\max} = w \times \frac{D}{q_o a^4} \times 10^3 = -4.062, \quad (36)$$

where $D = Et^3/12(1 - \nu^2)$ represents the flexural rigidity.

A high-fidelity FEM analysis simulates the analytical solution and the corresponding deformation profiles (see Figure 11A). The normalized maximum out-of-plane displacement at the plate's center is obtained as $\bar{w}_{\max} = -4.061$, closely matching the analytical solution of Equation (36). Since the deformation is purely due to bending, the strain distribution is anti-symmetric about the mid-plane. With no mid-plane stretching, surface strain values differ only in sign across the thickness. Therefore, strain measurements are needed only on one of the plate surfaces (e.g., $z = \pm t/2$). These discrete strain measures are used in the iFEM analysis to validate the iKS3 inverse element.

The iKS3 inverse element, using a 10×10 discretization, reconstructs the dimensionless transverse displacement with an absolute error of only 0.14% at maximum displacement (see Figure 11B), nearly indistinguishable from the high-fidelity FEM solution. Similarly, the iMIN3 inverse element provides a

displacement field in agreement with the reference solution, as can be seen in Figure 11C. However, the iMIN3 element shows slower convergence for thin plates, requiring a finer 40×40 discretization to achieve comparable accuracy. It yields a 0.24% absolute error in predicting maximum displacement. The improved continuity of the discrete Kirchhoff shape functions in the iKS3 formulation allows for a coarser discretization, accurately capturing bending behavior while maintaining iFEM accuracy.

Figure 12 highlights iFEM convergence trends for the iKS3 and iMIN3 inverse elements. It shows that the iFEM solution converges toward the analytical solution as the number of elements increases. Notably, the iKS3 element converges faster, requiring fewer elements to reconstruct the bending response accurately. This efficiency is crucial for real-time monitoring of dynamic structural changes, allowing for timely damage detection with reduced computational costs. The iKS3 element's reduced need for onboard sensors enhances flexibility in sensor placement and minimizes SHM costs. Thus, the iKS3 element offers improved practicality and effectiveness for ensuring structural safety and reliability in thin shell structures. Table 2 summarizes the analysis details for Case II.

3.3 | General Loading (Case - III)

A general loading condition is considered for a curved thin shell structure. The pinched cylinder with diaphragm boundary conditions is a well-known benchmark problem, representing one of the most challenging tests for both inextensional bending modes and complex membrane states. This case is part of the obstacle course for shell elements [31]. The cylinder, with a length $l = 600$, radius $r = 300$, and thickness $t = 3$, is subjected to a unit point load $P = 1$ at the center on opposite sides, as shown in Figure 13. The cylinder's ends are equipped with rigid diaphragms, and its material properties are $E = 3.0 \times 10^6$ and $\nu = 0.3$. Due to symmetry, only one octant of the cylinder is analyzed using both FEM and iFEM approaches (see Figure 13). Symmetric boundary conditions are applied along sides AB, BC, and CD, while rigid diaphragm conditions are imposed at the AB end. A radial point load of $-P/4$ is applied at point C. The reference solution for this case yields a maximum transverse displacement of $w_z = -1.824 \times 10^{-5}$ at the point of load application.

First, a high-fidelity FEM analysis is performed to replicate the reference result. The numerical solution converges steadily to the reference value, with a maximum radial displacement of -1.828×10^{-5} . This displacement is highly localized at the node where the radial point load is applied, as shown in Figure 14A.

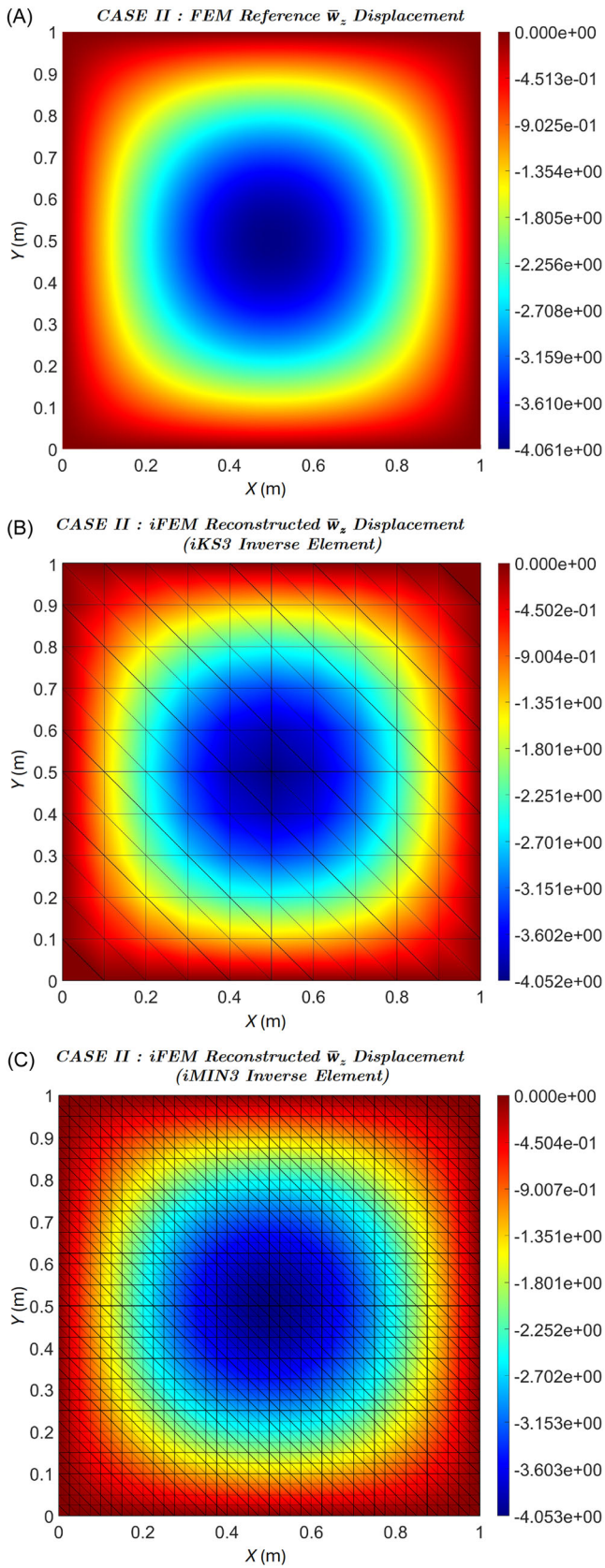


FIGURE 11 | Case II - Transverse displacement profiles: (A) FEM^{Ref}, (B) iFEM iKS3, and (C) iFEM iMIN3.

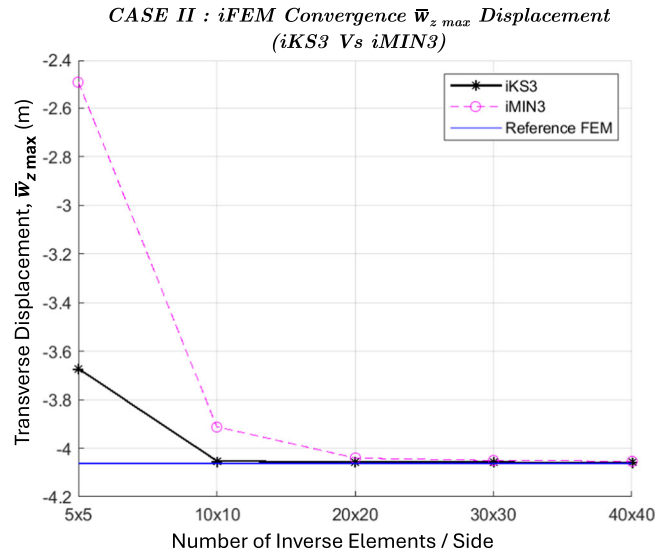


FIGURE 12 | Case II - Influence of inverse discretization on reconstructed transverse displacement.

TABLE 2 | Analysis details of Case - II.

Analysis	Sensors	Max \bar{w}_z	Error [\bar{w}_z]
Reference FEM	-----	-4.061	0.02% abs
iFEM-iKS3	10 × 10	-4.052	0.24% abs
iFEM-iMIN3	10 × 10	-3.911	3.71% abs
iFEM-iMIN3	40 × 40	-4.053	0.22% abs
Analytical solution [30]		-4.062	

CASE III: Pinched Cylinder Benchmark

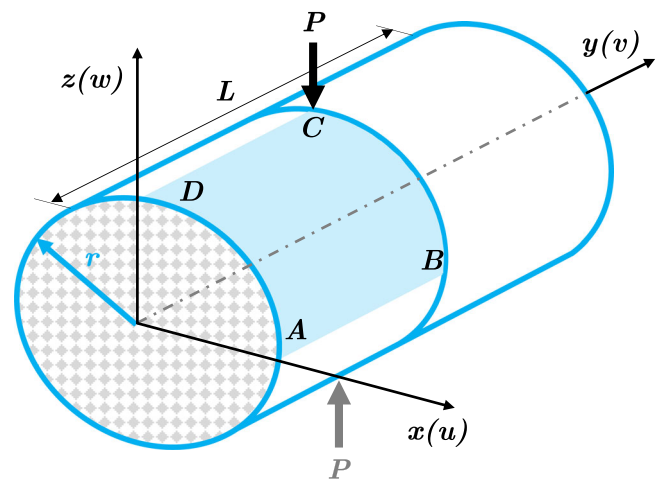


FIGURE 13 | Pinched cylinder with diaphragm boundary conditions.

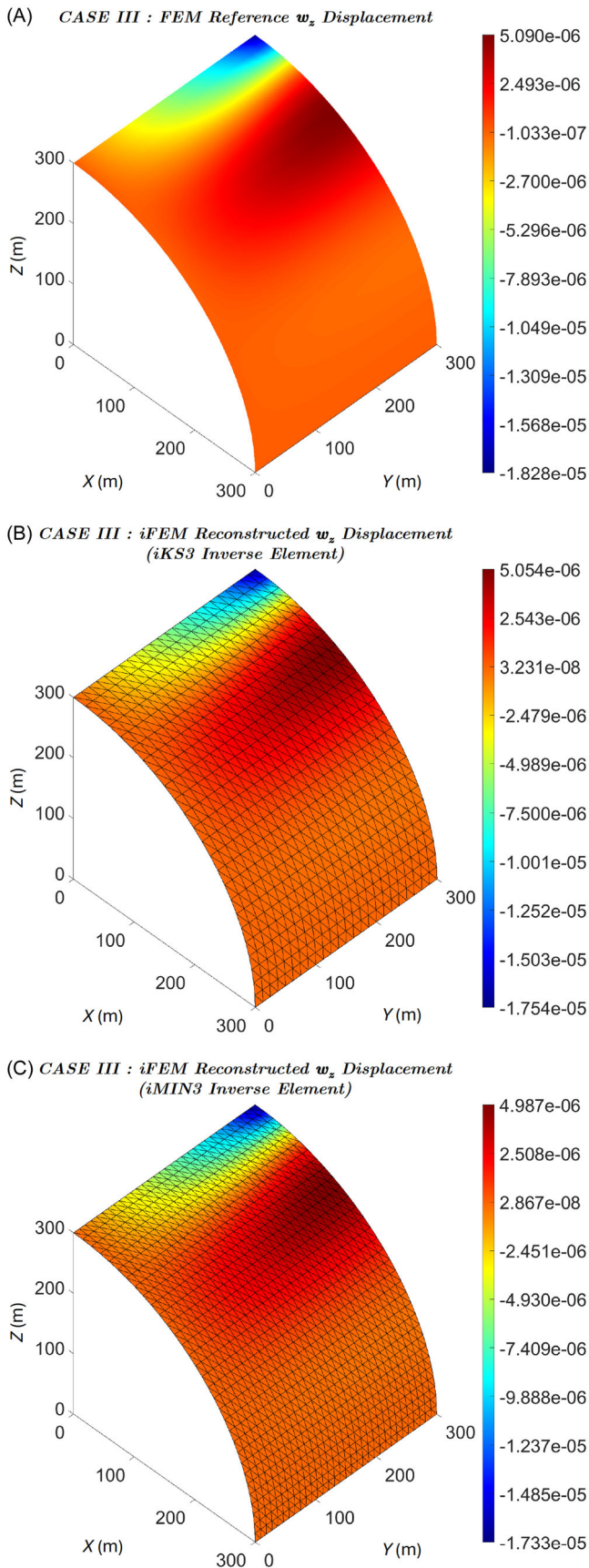


FIGURE 14 | Case III - Transverse displacement profiles: (A) FEM^{Ref}, (B) iFEM iKS3, and (C) iFEM iMIN3.

The concentration of the load causes significant deformation at this point. Synthetic strain data, derived from the displacement profile of the high-fidelity model, are used for the subsequent iFEM analysis. Accurate deformation reconstruction requires discrete strain measures on both surfaces for three-dimensional structures.

A comparison between the iKS3 and iMIN3 inverse shell elements highlights the efficacy of iKS3 in terms of accuracy and sensor efficiency. The iKS3 element (using a 24×24 discretization arrangement) reconstructs a maximum radial deflection of -1.754×10^{-5} , resulting in an absolute error of 4.04% despite the complexity of the problem (Figure 14B). In contrast, the iMIN3 element, even with a finer 32×32 discretization, produces a slightly lower maximum radial displacement of -1.733×10^{-5} , with a higher absolute error of 5.19% (Figure 14C). This comparison highlights the efficiency and accuracy of the iKS3 inverse element in achieving accurate displacement reconstructions with fewer inverse elements. Since the maximum displacement occurs in a highly localized region, finer discretization is required for accurate displacement reconstruction. Interpolation of discrete strain data (available at centroids) to other locations within inverse elements may introduce slight interpolation errors in regions with steep displacement gradients. A finer mesh is, therefore, essential to capture these localized effects. Table 3 summarizes the analysis details for Case III.

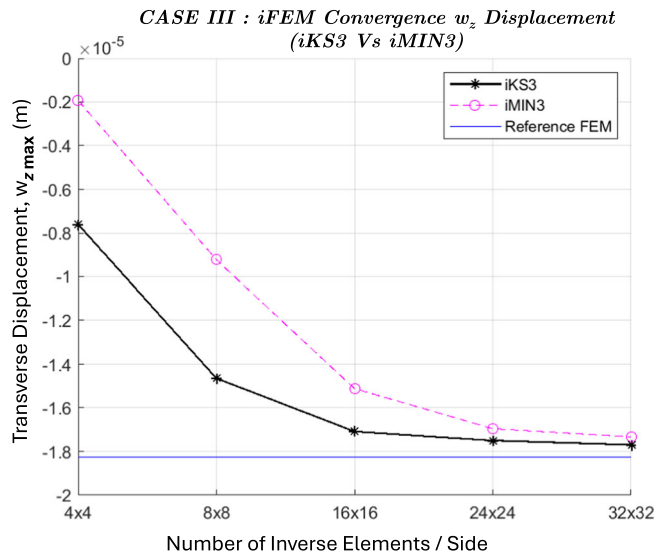
The influence of inverse discretization on the accuracy of displacement profile reconstruction is also investigated for both iKS3 and iMIN3 inverse shell elements (Figure 15). As the number of inverse elements increases, both elements gradually converge to the reference solution. The convergence trend lines reveal that the iKS3 element demonstrates a faster convergence rate than iMIN3, highlighting its effectiveness in reconstructing an accurate displacement field. Also, the iKS3 element requires fewer inverse elements while offering improved computational efficiency, making it a cost-effective choice. These advantages emphasize the potential applications of the proposed inverse formulation for SHM implementations designed for thin shell structures.

4 | SHM Applications of the iKS3 Inverse Element

After the successful numerical validation of the proposed inverse formulation, the iKS3 inverse shell element is now applied to real-world SHM tasks, including shape-sensing, defect identification, and damage assessment. In industrial SHM applications, several factors influence the determination of the optimal number of sensors for shape-sensing, including available space for sensor installation, budgetary constraints, structural health, and the balance between computational accuracy and efficiency. Achieving an optimal sensor arrangement requires optimizing the iFEM framework, which involves optimal inverse element discretization, selecting suitable sensor locations, and adjusting weighting functions in the error functional. Because each structure experiences unique in-service loading conditions, there is no universal, closed-form solution for determining the optimal sensor arrangement across

TABLE 3 | Analysis details of Case - III.

Analysis	Sensors	Max \bar{w}_z	Error [\bar{w}_z]
Reference FEM	- - - - -	-1.828×10^{-5}	0.21% abs
iFEM-iKS3	24×24	-1.754×10^{-5}	4.04% abs
iFEM-iMIN3	24×24	-1.695×10^{-5}	7.27% abs
iFEM-iMIN3	32×32	-1.733×10^{-5}	5.19% abs
Reference solution [31]		-1.824×10^{-5}	

**FIGURE 15** | Case III - Influence of inverse discretization on reconstructed transverse displacement.

different systems. However, advanced techniques such as sensor fusion and signal processing can help improve the robustness of iFEM under practicable sensor arrangements.

The following numerical cases use sparse sensor arrangements with coarser discretizations and fewer sensors than denser arrangements used for numerical validation. The aim is to evaluate the robustness of the iFEM algorithm with a limited number of onboard strain sensors. A standardized analysis setup assumes strain sensors at the centroid of each inverse element to compute synthetic strain data. When discrete strain measures are available within an inverse element for sparse sensor arrangement, the weighting coefficients are set to unity ($w_e = w_k = 1$). Conversely, when these measures are unavailable, the coefficients are fixed to ($w_e = w_k = 10^{-3}$). While both sensor locations and weighting functions are integral to the variational formulation of iFEM, their fixed values facilitate an intuitive interpretation of the iFEM results.

4.1 | Shape-Sensing of a Stiffened Panel

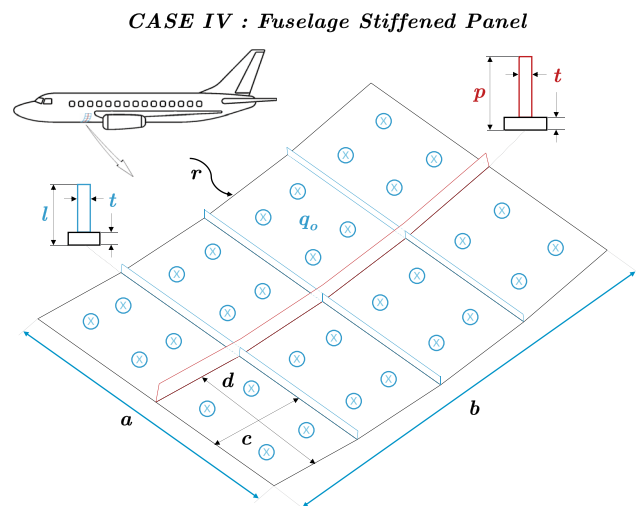
Stiffened panels are extensively utilized in airframes and barge structural systems due to their high load-bearing capacity, lightweight design, and resistance to buckling and fatigue. These panels efficiently distribute loads and withstand dynamic

forces, significantly enhancing structural integrity. Their superior strength-to-weight ratio makes them essential in applications demanding aerodynamic or hydrodynamic efficiency and structural resilience.

Consider a wide-body aircraft operating at a cruise altitude of 39 000 ft, with cabin pressure maintained at an equivalent altitude of 8000 ft, creating a pressure differential of 8.06 psi (or 0.56 bar). Under these conditions, the fuselage experiences a uniform pressure load of 55 571.71 Pa, accurately simulating the operational scenarios where cabin pressurization induces deformation in the fuselage structure. The aircraft fuselage consists of thin, stiffened curved panels that are securely fastened and sealed along their edges to the main airframe. This arrangement effectively simulates a clamped boundary condition (BC) on all sides to withstand aerodynamic loads and internal pressures during flight.

The curved stiffened panel geometry, as shown in Figure 16, has a radius of $r = 1.960$ m and a thickness of $t = 0.002$ m, with dimensions $a = 0.563$ m, $b = 0.795$ m, $c = 0.198$ m, and $d = 0.281$ m. Three stiffeners, each with a height of $l = 0.019$ m, are positioned along the width of the panel, reinforced by a main stiffener at the center that extends along its length, with a height of $p = 0.038$ m. The panel is made from Aluminum Alloy 2024-T3, a material widely used in aerospace applications due to its favorable strength-to-weight ratio. The material properties include Young's modulus of $E = 73.1$ GPa and Poisson's ratio of $\nu = 0.33$.

Initially, the fuselage stiffened panel is analyzed using a high-fidelity FEM model composed of 2080 structured triangular elements. Under the given conditions, the stiffened panel experiences significant transverse deformations (bulging), primarily between the frames and stringers. Figure 17A illustrates the transverse displacement profile of the stiffened panel, highlighting a maximum displacement of 1.739 mm at its center. The displacement field obtained from the high-fidelity FEM model generates synthetic strain data and serves as the reference solution for subsequent iFEM analysis.

**FIGURE 16** | Case IV - Aircraft fuselage stiffened panel under cabin pressurization.

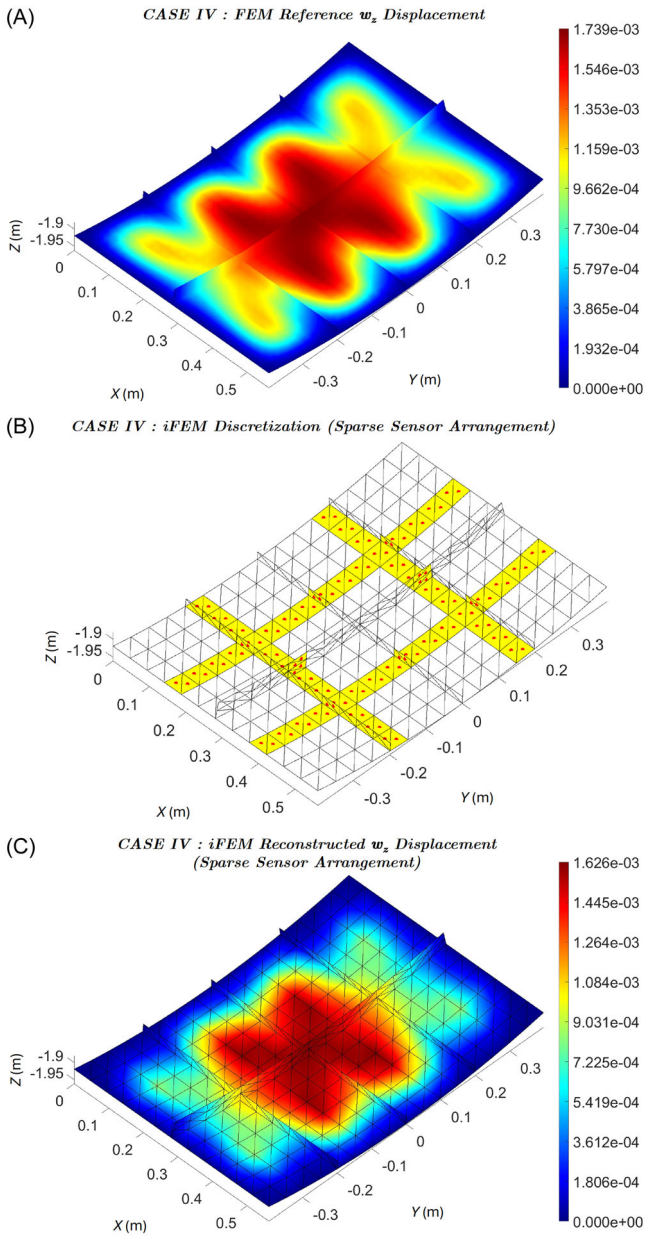


FIGURE 17 | Case IV - Transverse displacement profile: (A) FEM^{Ref}, (B) Sparse Sensor Arrangement, and (C) iFEM iKS3 under a Sparse Sensor Arrangement.

The iFEM framework uses a coarse discretization scheme for the shape-sensing analysis, utilizing 520 iKS3 inverse shell elements to map the entire geometric domain (illustrated in Figure 17B). Only 120 inverse elements with discrete strain measures are used to reconstruct the displacement field, simulating a practical sensor arrangement. The inverse elements with discrete strain measures are highlighted in yellow (see Figure 17B), with sensor locations marked by red dots at the centroids of these elements.

The reconstructed transverse displacement contour depicts close agreement with the reference displacement contour obtained from the FEM solution, as depicted in Figure 17C. The maximum reconstructed transverse displacement shows an absolute error of only 6.49%, showing the effectiveness of the iKS3 inverse shell element in reliable reconstruction of the

displacement field with fewer onboard sensors. The proposed inverse formulation offers advantages over FSDT-based inverse elements in addressing the challenges of thin aerospace structures. It provides computational efficiency and requires fewer sensors for shape-sensing applications. While the sparsely arranged sensors in this study have proven effective for this scenario, they are intended to inspire further designs for applications involving more complex structures.

4.2 | Damage Assessment

In practical engineering applications, not all structural defects present apparent geometric discontinuities. Material degradation, mainly due to cyclic loading, is a significant concern in the aerospace, naval, and energy sectors. Repeated stress induces fatigue, causing gradual deterioration of material properties. These changes are often latent, making them difficult to detect early and posing serious risks to structural integrity. Therefore, an effective SHM system can detect early signs of material degradation, facilitate timely maintenance, and ensure the reliability and safety of structures.

Consider a rectangular plate with length $b = 0.3$ m, width $a = 0.1$ m, and thickness $t = 0.001$ m. The plate is fixed along the left and right edges, and a uniform transverse pressure $q_0 = 1000$ Pa is applied across its surface, as depicted in Figure 18. The plate is assumed to be made of an isotropic material with Young's modulus $E = 200$ GPa and Poisson's ratio $\nu = 0.3$. A material degradation defect is modeled at the center of the plate, as illustrated in Figure 18, representing a region with reduced material stiffness. This setup is used to analyze the structural response of the plate under transverse loading conditions, accounting for the effects of material degradation.

To accurately model the defective domain in finite element analysis, a degradation factor λ , ranging between 0 and 1, is used. A healthy material corresponds to $\lambda = 1$, while $0 < \lambda < 1$ represents degraded material. In this case, $\lambda = 0.75$ is used in high-fidelity FEM analysis, incorporated into the stiffness matrix to reflect the material degradation defect. The displacement field obtained is then used to generate synthetic strain measures for iFEM analysis.

The iFEM results for transverse deflection w_z and bending rotations θ_x and θ_y are shown in Figure 19A–C. The transverse displacement w_z and rotation θ_y show slight deviations in areas

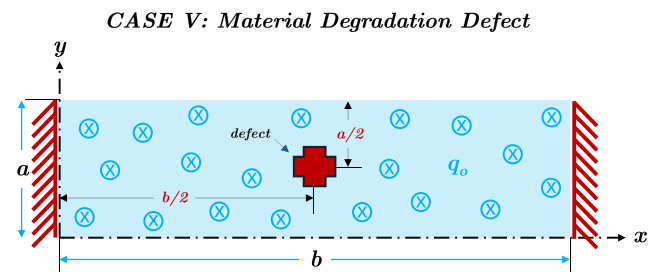


FIGURE 18 | Case V - Material degradation defect under transverse loading.

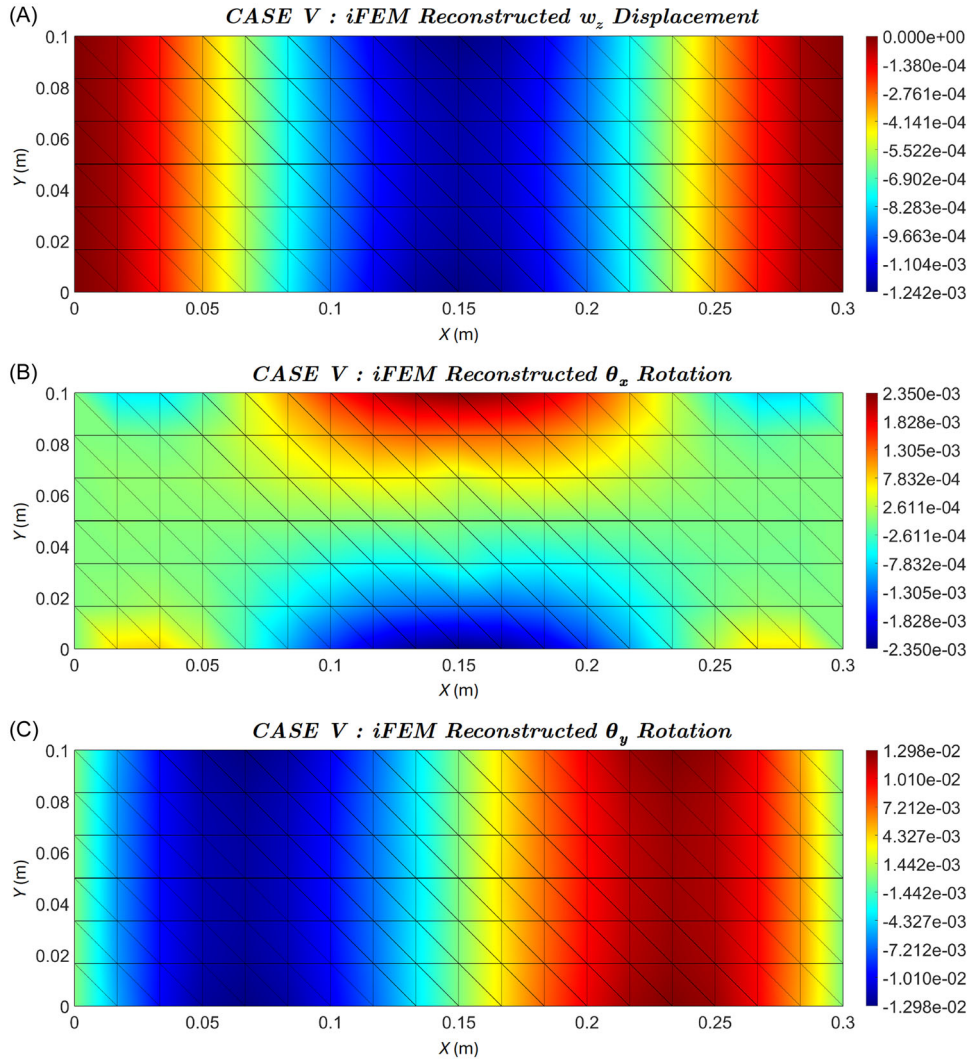


FIGURE 19 | Case V - iFEM iKS3 reconstructed displacement profiles: (A) transverse displacement, (B) bending rotation θ_x , and (C) bending rotation θ_y .

affected by the defect, whereas θ_x shows a more pronounced variation. The defect sensitivity of these displacement variables depends on the defect's position, orientation, and the applied boundary and loading conditions. Equivalent von Mises strain contours also help identify and quantify subtle defects when comparing reconstructed displacement profiles of healthy and defective structures. The equivalent von Mises strains are computed using the following expression:

$$\varepsilon_{vm} = \sqrt{(\varepsilon_1)^2 - \varepsilon_1\varepsilon_2 + (\varepsilon_2)^2}, \quad (37)$$

where ε_1 and ε_2 can be calculated as

$$\begin{cases} \varepsilon_1 = \frac{\varepsilon_{xx} + \varepsilon_{yy}}{2} + \sqrt{\left(\frac{\varepsilon_{xx} - \varepsilon_{yy}}{2}\right)^2 + \left(\frac{\gamma_{xy}}{2}\right)^2} \\ \varepsilon_2 = \frac{\varepsilon_{xx} + \varepsilon_{yy}}{2} - \sqrt{\left(\frac{\varepsilon_{xx} - \varepsilon_{yy}}{2}\right)^2 + \left(\frac{\gamma_{xy}}{2}\right)^2} \end{cases}$$

Here, ε_{xx} , ε_{yy} , and γ_{xy} are the in-plane normal and shear strain components. These von Mises strain contours enable the detection of localized defects by revealing strain anomalies in the material.

The von Mises strain contours for both defective and healthy structures are presented in Figure 20A,B. Comparison of these contours aids in identifying and quantifying the defective region at the plate's center. However, the use of damage index (DI) criteria based on von Mises strains offers more precise insights into the defect's location and size, leading to a more thorough structural integrity evaluation. This DI criterion is general enough to assess a variety of structural defects, including material degradation, discontinuities (such as cracks and voids), delamination, and corrosion. The DI can be calculated using the following expression:

$$DI(\varepsilon_{vm}) = \left| \frac{\varepsilon_{vm} - \varepsilon_{vm}^*}{\varepsilon_{vm}^{\max}} \right| \times 100\%, \quad (38)$$

where ε_{vm} represents the equivalent von Mises strain calculated from the iFEM framework for an intact structure and ε_{vm}^{\max} denotes the maximum reconstructed von Mises strain observed during the analysis. ε_{vm}^* refers to the von Mises strain of the degraded structure. In SHM applications, the DI is a valuable metric for quantifying the severity of material degradation, facilitating informed decisions for preventive maintenance to ensure structural safety and reliability.

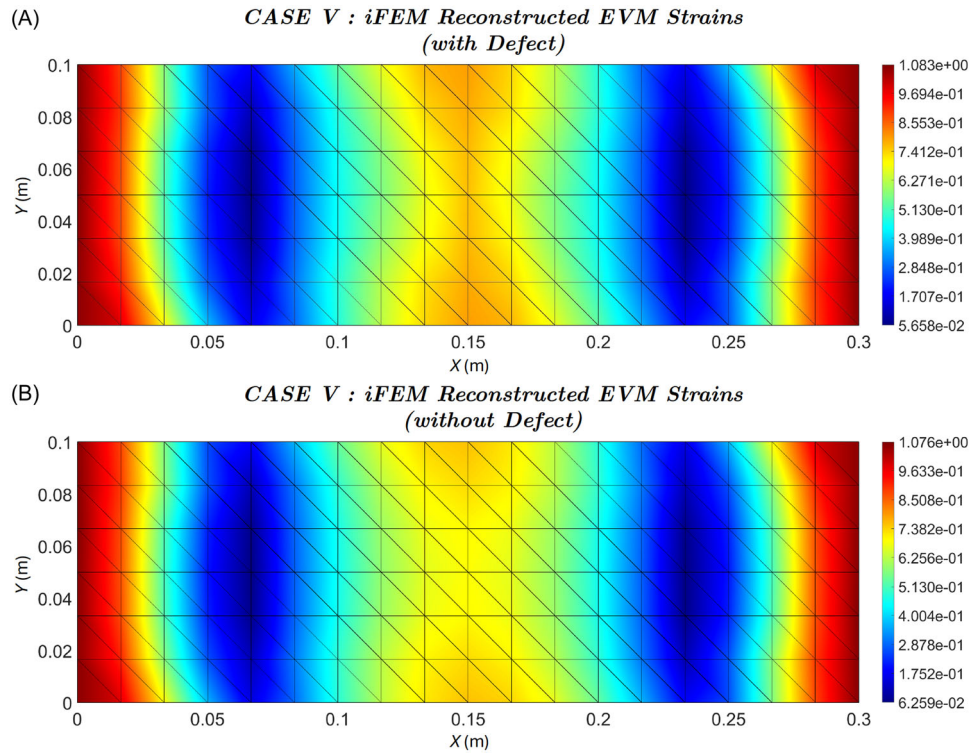


FIGURE 20 | Case V - iFEM iKS3 reconstructed equivalent von Mises strains (A) with defect and (B) without defect.

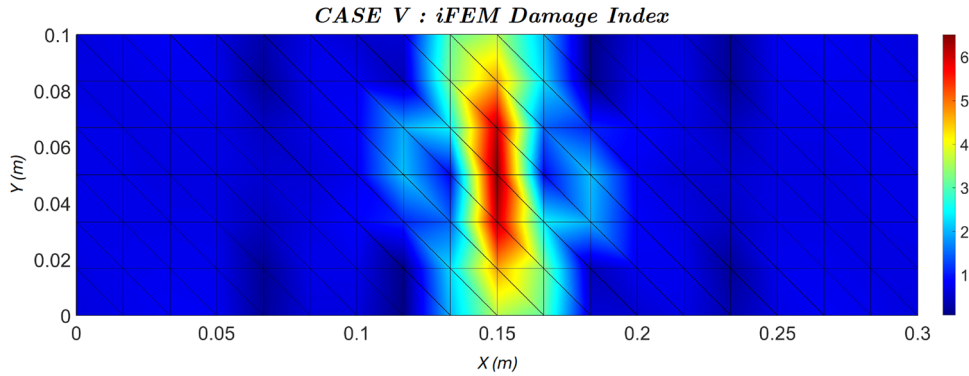


FIGURE 21 | Case V - iFEM iKS3 reconstructed damage index (DI) profile.

Figure 21 illustrates the DI contour for this case, computed using Equation (38). The contour effectively pinpoints the location of material degradation and enables preliminary sizing of the defect. Furthermore, DI values provide insight into the structural integrity, where a $DI \leq 10$ is generally considered minor damage. While minor damage may not immediately compromise structural integrity, it requires continuous monitoring. This analysis highlights the utility of the iKS3 inverse shell element in assessing structural health and identifying areas in need of preventive maintenance, thereby contributing to the overall reliability and safety of thin shell structures.

5 | Conclusion

This study uses discrete Kirchhoff assumptions to introduce a three-node triangular inverse shell element (iKS3) for thin plates and shell structures widely used in aerospace, naval, and

energy sectors. Triangular elements offer excellent flexibility in handling structured and unstructured discretizations for regular and complex built-up structures. The inverse formulation neglects transverse shear effects in accordance with CPT assumptions, simplifying the error functional and enhancing computational efficiency compared to existing inverse elements based on the FSDT. Incorporating the drilling DOF improves inter-element continuity and compatibility between membrane and bending behaviors.

The proposed inverse formulation is subjected to numerical validation against benchmark problems under in-plane, bending, and mixed-loading conditions. Its full-field displacement reconstruction capability is also compared to the existing iMIN3 inverse shell element. The iKS3 formulation demonstrates numerical stability and outperforms the iMIN3 inverse shell element in convergence rates for pure bending and general loading conditions. As a result, the iKS3 inverse element offers

computational advantage and improved accuracy while reducing the number of onboard sensors needed for shape-sensing applications.

After extensive numerical validation, the iKS3 inverse shell element is further evaluated for SHM applications, considering real-world industrial cases. The inverse formulation reveals reliable accuracy in shape-sensing and defect resolution, successfully detecting and quantifying material degradation defects. These capabilities are crucial for modern health monitoring systems, enabling efficient maintenance scheduling while ensuring structural reliability and safety. For thin shell structures, the iKS3 inverse shell element, characterized by its straightforward formulation and computational efficiency, presents significant potential for industrial SHM applications to reduce sensor requirements and minimize overall project costs.

Acknowledgments

The authors have nothing to report.

Conflicts of Interest

The authors declare no conflicts of interest.

Data Availability Statement

The data that support the findings of this study are available from the corresponding author upon reasonable request.

References

1. S. Hassani and U. Dackermann, "A Systematic Review of Advanced Sensor Technologies for Non-Destructive Testing and Structural Health Monitoring," *Sensors* 23, no. 4 (2023): 2204.
2. H. Guo, X. Zhuang, and T. Rabczuk, "A Deep Collocation Method for the Bending Analysis of Kirchhoff Plate," *Computers, Materials & Continua* 59, no. 2 (2019): 433–456.
3. E. Samaniego, C. Anitescu, S. Goswami, et al., "An Energy Approach to the Solution of Partial Differential Equations in Computational Mechanics via Machine Learning: Concepts, Implementation and Applications," *Computer Methods in Applied Mechanics and Engineering* 362 (2020): 112790.
4. X. Zhuang, H. Guo, N. Alajlan, H. Zhu, and T. Rabczuk, "Deep Autoencoder Based Energy Method for the Bending, Vibration, and Buckling Analysis of Kirchhoff Plates With Transfer Learning," *European Journal of Mechanics - A/Solids* 87 (2021): 104225.
5. C. Wang, Q. Xiao, Z. Zhou, et al., "A Data-Assisted Physics-Informed Neural Network (DA-PINN) for Fretting Fatigue Lifetime Prediction," *International Journal of Mechanical System Dynamics* 4 (2024): 361–373.
6. W. L. Ko, W. L. Richards, and V. T. Tran, *Displacement Theories for In-Flight Deformed Shape Predictions of Aerospace Structures* (NASA, 2007).
7. W. L. Ko, W. L. Richards, and V. T. Fleischer, *Applications of Ko Displacement Theory to the Deformed Shape Predictions of the Doubly-Tapered Ikhana Wing* (NASA, 2009).
8. G. Foss and E. Haugse, "Using Modal Test Results to Develop Strain to Displacement Transformations." in *Proceedings of the 13th International Modal Analysis Conference*, Vol. 2460 (NASA, 1995), 112.
9. M. Gopinathan, G. A. Pajunen, P. S. Neelakanta, and M. Arockaisamy, "Recursive Estimation of Displacement and Velocity in a Cantilever Beam

Using a Measured Set of Distributed Strain Data," *Journal of Intelligent Material Systems and Structures* 6, no. 4 (1995): 537–549.

10. A. C. Pisoni, C. Santolini, D. E. Hauf, and S. Dubowsky, "Displacements in a Vibrating Body by Strain Gage Measurements," in *Proceedings—SPIE the International Society for Optical Engineering* (Citeseer, 1995), 119.
11. S. Shkarayev, *An Inverse Interpolation Method Utilizing In-flight Strain Measurements for Determining Loads and Structural Response of Aerospace Vehicles* (NASA, 2001). 3rd int. Workshop on Structural Health Monitoring.
12. J. S. Alexander Tessler *A Variational Principle for Reconstruction of Elastic Deformations in Shear Deformable Plates and Shells* (Report Number: NASA/TM-2003-2 12445), (NASA, 2003).
13. M. Gherlone, P. Cerracchio, and M. Mattone, "Shape Sensing Methods: Review and Experimental Comparison on a Wing-Shaped Plate," *Progress in Aerospace Sciences* 99 (2018): 14–26.
14. A. Tessler and J. L. Spangler, *Inverse Fem for Full-field Reconstruction of Elastic Deformations in Shear Deformable Plates and Shells. 2nd European Workshop on Structural Health Monitoring* (NASA, 2004).
15. A. Kefal, E. Oterkus, A. Tessler, and J. L. Spangler, "A Quadrilateral Inverse-Shell Element With Drilling Degrees of Freedom for Shape Sensing and Structural Health Monitoring," *Engineering Science and Technology, an International Journal* 19, no. 3 (2016): 1299–1313.
16. A. Kefal, "An Efficient Curved Inverse-Shell Element for Shape Sensing and Structural Health Monitoring of Cylindrical Marine Structures," *Ocean Engineering* 188 (2019): 106262.
17. I. Khalid, Z. A. Qureshi, H. A. Khan, S. Oterkus, and E. Oterkus, "A Quadrilateral Inverse Plate Element for Real-Time Shape-Sensing and Structural Health Monitoring of Thin Plate Structures," *Computers & structures* 305 (2024): 107551.
18. A. Kefal and E. Oterkus, "Isogeometric iFEM Analysis of Thin Shell Structures," *Sensors* 20, no. 9 (2020): 2685.
19. Y. Dirik, S. Oterkus, and E. Oterkus, "Isogeometric Mindlin-Reissner Inverse-Shell Element Formulation for Complex Stiffened Shell Structures," *Ocean Engineering* 305 (2024): 118028.
20. C. De Mooij, M. Martinez, and R. Benedictus, "iFEM Benchmark Problems for Solid Elements," *Smart Materials and Structures* 28, no. 6 (2019): 065003.
21. A. Kefal, A. Tessler, and E. Oterkus, "An Enhanced Inverse Finite Element Method for Displacement and Stress Monitoring of Multi-layered Composite and Sandwich Structures," *Composite Structures* 179 (2017): 514–540.
22. I. Khalid, Z. A. Qureshi, H. Q. Ali, S. Oterkus, and E. Oterkus, "Structural Health Monitoring of Pre-Cracked Structures Using an In-plane Inverse Crack Tip Element," *International Journal of Mechanical System Dynamics* 4 (2024): 406–426.
23. O. Eugenio, *Structural Analysis With the Finite Element Method: Linear Statics*, 1st ed. (Springer, 2009).
24. J. L. Batoz, K. J. Bathe, and L. W. Ho, "A Study of Three-Node Triangular Plate Bending Elements," *International Journal for Numerical Methods in Engineering* 15, no. 12 (1980): 1771–1812.
25. D. J. Allman, "A Compatible Triangular Element Including Vertex Rotations for Plane Elasticity Analysis," *Computers & Structures* 19, no. 1–2 (1984): 1–8.
26. M. A. Abdollahzadeh, H. Q. Ali, M. Yildiz, and A. Kefal, "Experimental and Numerical Investigation on Large Deformation Reconstruction of Thin Laminated Composite Structures Using Inverse Finite Element Method," *Thin-Walled Structures* 178 (2022): 109485.
27. E. J. Miller, R. Manalo, and A. Tessler, *Full-Field Reconstruction of Structural Deformations and Loads From Measured Strain Data on a Wing Using the Inverse Finite Element Method* (NASA, 2016).

28. D. J. Allman, "A Quadrilateral Finite Element Including Vertex Rotations for Plane Elasticity Analysis," *International Journal for Numerical Methods in Engineering* 26, no. 3 (1988): 717–730.

29. A. Ibrahimbegovic, R. L. Taylor, and E. L. Wilson, "A Robust Quadrilateral Membrane Finite Element With Drilling Degrees of Freedom," *International Journal for Numerical Methods in Engineering* 30, no. 3 (1990): 445–457.

30. S. Timoshenko and J. Goodier, *Theory of Elasticity*, Vol. 1 (New York: Inc., 1951), 35–39.

31. T. Belytschko, H. Stolarski, W. K. Liu, N. Carpenter, and J. S. J. Ong, "Stress Projection for Membrane and Shear Locking in Shell Finite Elements," *Computer Methods in Applied Mechanics and Engineering* 51, no. 1–3 (1985): 221–258.

Appendix A

Triangular Basis Functions

The explicit forms of linear basis functions used for the triangular inverse element are presented here. These basis functions are utilized for geometric mapping and interpolation of the in-plane translational displacement variables.

$$N_1(\xi, \eta) = 1 - \xi - \eta, \quad (\text{A1a})$$

$$N_2(\xi, \eta) = \xi, \quad (\text{A1b})$$

$$N_3(\xi, \eta) = \eta, \quad (\text{A1c})$$

where ξ and η are the natural barycentric coordinates of the three-node triangular element.

Similarly, the explicit forms of quadratic basis functions for the six-node triangular element are outlined below for interpolating out-of-plane displacement variables.

$$S_1(\xi, \eta) = \xi(2\xi - 1), \quad (\text{A2a})$$

$$S_2(\xi, \eta) = \eta(2\eta - 1), \quad (\text{A2b})$$

$$S_3(\xi, \eta) = (\eta + \xi - 1)(2\eta + 2\xi - 1), \quad (\text{A2c})$$

$$S_4(\xi, \eta) = 4\xi\eta, \quad (\text{A2d})$$

$$S_5(\xi, \eta) = 4\eta(1 - \xi - \eta), \quad (\text{A2e})$$

$$S_6(\xi, \eta) = 4\xi(1 - \xi - \eta). \quad (\text{A2f})$$

Here, ξ and η are the natural barycentric coordinates of the six-node triangular element.

Appendix B

Drilling Rotation DOF

The anisoparametric shape functions L_i and M_i are crucial for capturing rotational DOF in finite element models. These functions allow accurate representation of drilling rotations and are defined as follows for the inverse triangular element:

$$L_1 = \frac{S_6 y_{13} - S_4 y_{21}}{8}, \quad (\text{B1a})$$

$$L_2 = \frac{S_4 y_{21} - S_5 y_{32}}{8}, \quad (\text{B1b})$$

$$L_3 = \frac{S_5 y_{32} - S_6 y_{13}}{8}, \quad (\text{B1c})$$

$$M_1 = \frac{-S_6 x_{13} + S_4 x_{21}}{8}, \quad (\text{B2a})$$

$$M_2 = \frac{-S_4 x_{21} + S_5 x_{32}}{8}, \quad (\text{B2b})$$

$$M_3 = \frac{-S_5 x_{32} + S_6 x_{13}}{8}. \quad (\text{B2c})$$

Here, S_4 to S_6 are basis functions for the six-node triangular element defined in Equations (A2d)–(A2f), and the nodal distances x_{ij} and y_{ij} defined as:

$$\begin{aligned} x_{13} &= x_1 - x_3, y_{31} = y_3 - y_1 \\ x_{21} &= x_2 - x_1, y_{21} = y_2 - y_1 \\ x_{32} &= x_3 - x_2, y_{23} = y_3 - y_3. \end{aligned}$$

Appendix C

Discrete Kirchhoff's Triangular Shape Functions

In this section, the shape function vectors \mathbf{H}^x and \mathbf{H}^y are defined in the local element coordinate system based on discrete Kirchhoff assumptions and proposed by Batoz et al. [24]. The anisoparametric shape functions satisfy continuity requirements for displacement and rotation across the element edges, which is crucial for accurate structural analysis, particularly for thin plates.

$$\mathbf{H}^x = \begin{bmatrix} 1.5(a_4 S_4 - a_6 S_6) \\ -(b_6 S_6 + b_4 S_4) \\ -(S_1 - c_6 S_6 - c_4 S_4) \\ 1.5(a_5 S_5 - a_4 S_4) \\ -(b_5 S_5 + b_4 S_4) \\ -(S_2 - c_5 S_5 - c_4 S_4) \\ 1.5(a_6 S_6 - a_5 S_5) \\ -(b_5 S_5 + b_6 S_6) \\ -(S_3 - c_5 S_5 - c_6 S_6) \end{bmatrix}, \quad (\text{C1})$$

$$\mathbf{H}^y = \begin{bmatrix} 1.5(d_4 S_4 - d_6 S_6) \\ -(-S_1 + e_6 S_6 + e_4 S_4) \\ -(b_6 S_6 - b_4 S_4) \\ 1.5(d_5 S_5 - d_4 S_4) \\ -(-S_2 + e_5 S_5 + e_4 S_4) \\ -(b_5 S_5 - b_4 S_4) \\ 1.5(d_6 S_6 - d_5 S_5) \\ -(-S_3 + e_5 S_5 + e_6 S_6) \\ -(b_5 S_5 - b_6 S_6) \end{bmatrix}. \quad (\text{C2})$$

Here, S_4 to S_6 are basis functions for the six-node triangular element defined in Equations (A2d)–(A2f). The shape functions are derived based on the local coordinates of the triangular element, denoted by subscripts p and q , representing the positions of the element nodes. The expressions for x_{pq} , y_{pq} , and r_{pq} define the geometric relationships between adjacent nodes, essential for ensuring the consistency and smoothness of the shape functions.

$$x_{pq} = x_p - x_q, \quad (\text{C3})$$

$$y_{pq} = y_p - y_q, \quad (\text{C4})$$

$$r_{pq} = x_{pq}^2 + y_{pq}^2, \quad (\text{C5})$$

where $r = 4, 5, 6$ when $pq = 12, 23, 31$

The coefficients $a_r, b_r, c_r, d_r,$ and e_r depend on the triangular's geometry and node positions.

$$a_r = -\frac{x_{pq}}{r_{pq}}, \tag{C6}$$

$$b_r = \frac{3}{4} \frac{x_{pq} y_{pq}}{r_{pq}}, \tag{C7}$$

$$c_r = \frac{x_{pq}^2 - 2y_{pq}^2}{4r_{pq}}, \tag{C8}$$

$$d_r = -\frac{y_{pq}}{r_{pq}}, \tag{C9}$$

$$e_r = \frac{y_{pq}^2 - 2x_{pq}^2}{4r_{pq}}. \tag{C10}$$

Appendix D

Coordinate Transformation System

Typically, two-dimensional shell elements, formulated by a superimposing membrane and bending components, are computationally efficient and relatively simple. In such formulations, the transformation between the element's local and global coordinate systems is crucial, particularly for the proposed inverse shell element. Given the position vectors between any two nodes within the element, the unit vectors defining the local coordinate system (x', y', z') can be determined using vector calculus.

The vector between two nodes i and j is defined as

$$\mathbf{V}_{ij}^e = \begin{Bmatrix} x_j - x_i \\ y_j - y_i \\ z_j - z_i \end{Bmatrix} = \begin{Bmatrix} x_{ij} \\ y_{ij} \\ z_{ij} \end{Bmatrix}. \tag{D1}$$

The corresponding unit vector is

$$\hat{\mathbf{v}}_{ij}^e = \frac{1}{l_{ij}^e} \begin{Bmatrix} x_{ij} \\ y_{ij} \\ z_{ij} \end{Bmatrix} = \frac{\mathbf{V}_{ij}^e}{\|\mathbf{V}_{ij}^e\|}, \tag{D2}$$

where l_{ij}^e is the length of the side between nodes i and j .

$$l_{ij}^e = \sqrt{(x_{ij}^2 + y_{ij}^2 + z_{ij}^2)}^e. \tag{D3}$$

First, the unit vector along the local z' axis is determined to define the local coordinate system. For the given triangular inverse element, this transverse local unit vector is calculated using the cross product of vectors \mathbf{V}_{12}^e and \mathbf{V}_{13}^e , which lie along nodes 1-2 and 1-3, respectively.

$$\hat{\mathbf{v}}_{z'}^e = \frac{\mathbf{V}_{12}^e \times \mathbf{V}_{13}^e}{\|\mathbf{V}_{12}^e \times \mathbf{V}_{13}^e\|} = \begin{Bmatrix} \lambda_{z'x} \\ \lambda_{z'y} \\ \lambda_{z'z} \end{Bmatrix}. \tag{D4}$$

The local y' axis is now defined by intersecting the element with a plane parallel to the global yz plane, and the unit vector along the local y' axis is

$$\hat{\mathbf{v}}_{y'}^e = \begin{Bmatrix} 0 \\ \lambda_{y'y} \\ \lambda_{y'z} \end{Bmatrix}. \tag{D5}$$

Here, the projection of x' onto the global y axis is zero. The unknown components $\lambda_{y'y}$ and $\lambda_{y'z}$ are determined by ensuring that the unit vector $\hat{\mathbf{v}}_{y'}^e$ maintains a length of unity:

$$(\lambda_{y'y}^e)^2 + (\lambda_{y'z}^e)^2 = 1 \tag{D6}$$

and the second necessary equation comes from the condition that the scalar product of the unit vectors $\hat{\mathbf{v}}_{y'}^e$ and $\hat{\mathbf{v}}_{z'}^e$ is zero. Additionally, the unit vectors $\hat{\mathbf{v}}_{y'}^e$ and $\hat{\mathbf{v}}_{z'}^e$ must be orthogonal, which provides the second equation:

$$\lambda_{y'y}^e \lambda_{z'y}^e + \lambda_{y'z}^e \lambda_{z'z}^e = 0. \tag{D7}$$

From Equations (D6) and (D7), the unknown components ($\lambda_{y'y}, \lambda_{y'z}$) of the unit vector $\hat{\mathbf{v}}_{y'}^e$ can be obtained easily.

$$\lambda_{y'y}^e = \frac{1}{\sqrt{1 + \left(\frac{\lambda_{z'z}^e}{\lambda_{z'y}^e}\right)^2}}, \tag{D8}$$

$$\lambda_{y'z}^e = \frac{1}{\sqrt{1 + \left(\frac{\lambda_{z'y}^e}{\lambda_{z'z}^e}\right)^2}}. \tag{D9}$$

Finally, the unit vector along the local x' axis is obtained by determining the cross product of $\hat{\mathbf{v}}_{y'}^e$ and $\hat{\mathbf{v}}_{z'}^e$.

$$\hat{\mathbf{v}}_{x'}^e = \hat{\mathbf{v}}_{y'}^e \times \hat{\mathbf{v}}_{z'}^e = \begin{Bmatrix} \lambda_{x'x} \\ \lambda_{x'y} \\ \lambda_{x'z} \end{Bmatrix}. \tag{D10}$$

These local unit vectors $\hat{\mathbf{v}}_{x'}^e, \hat{\mathbf{v}}_{y'}^e, \hat{\mathbf{v}}_{z'}^e$ define the direction cosines that describe the orientation of the local coordinate system [x', y', z'] relative to the global coordinate system [x, y, z]. The transformation matrix \mathbf{T} can be assembled using Equations (D4), (D5), and (D10).

$$\mathbf{T} = \begin{Bmatrix} \lambda_{x'x}^e & \lambda_{x'y}^e & \lambda_{x'z}^e \\ \lambda_{y'x}^e & \lambda_{y'y}^e & \lambda_{y'z}^e \\ \lambda_{z'x}^e & \lambda_{z'y}^e & \lambda_{z'z}^e \end{Bmatrix}. \tag{D11}$$

Here, \mathbf{T} is a 3×3 matrix that transforms global coordinates [x, y, z] into local coordinates [x', y', z'] = $\mathbf{T}[x, y, z]$. This transformation is critical in shell element formulations to ensure accurate alignment between local and global coordinate systems.

After computing the local stiffness matrix \mathbf{k}'^e , it is transformed into a global stiffness \mathbf{k}^e matrix using the element transformation matrix \mathbf{T}^e .

$$\mathbf{k}^e = [\mathbf{T}^e]^T \mathbf{k}'^e [\mathbf{T}^e]. \tag{D12}$$

For the entire iKS3 inverse shell element, which has six DOFs per node, the complete element transformation matrix is represented as

$$\mathbf{T}^e = \begin{bmatrix} \mathbf{T} & & & & & \\ & \mathbf{T} & & & & \\ & & \mathbf{T} & & & \\ & & & \mathbf{T} & & \\ & & & & \mathbf{T} & \\ & & & & & \mathbf{T} \\ & & & & & & \mathbf{0} \\ & & & & & & & \mathbf{T} \\ & & & & & & & & \mathbf{T} \\ & & & & & & & & & \mathbf{T} \\ & & & & & & & & & & \mathbf{T} \\ & & & & & & & & & & & \mathbf{T} \end{bmatrix}. \quad (\text{D13})$$

This 18×18 block-diagonal matrix \mathbf{T}^e is used to transform local element stiffness matrices into the global coordinate system. Its structure is essential for accurately mapping the local stiffness contributions to the global system, especially in three-dimensional problems where each node has six DOFs (three translations and three rotations).